Article:
Lamy-Mendes, A, Malfait, WJ, Sadeghpour, A orcid.org/0000-0002-0475-7858 et al. (3 more authors) (2021) Influence of 1D and 2D carbon nanostructures in silica-based aerogels. Carbon, 180. pp. 146-162. ISSN 0008-6223

https://doi.org/10.1016/j.carbon.2021.05.004

Influence of 1D and 2D carbon nanostructures in silica-based aerogels

Alyne Lamy-Mendes [1,2], Wim J. Malfait [3], Amin Sadeghpour [4,5], Ana V. Girão [2], Rui F. Silva [2] and Luísa Durães [1*].

1 - University of Coimbra, CIEPQPF, Department of Chemical Engineering, 3030-790 Coimbra, Portugal

2 - CICECO, Aveiro Institute of Materials, Department of Materials and Ceramic Engineering, University of Aveiro, 3810-193 Aveiro, Portugal

3 - Laboratory for Building Energy Materials and Components, Swiss Federal Laboratories for Materials Science and Technology, Empa, Dübendorf, Switzerland

4 - School of Food Science and Nutrition, University of Leeds, Leeds, LS2 9JT, United Kingdom

5 - Empa, Swiss Federal Laboratories for Materials Science and Technology, Center for X-Ray Analytics, St. Gallen, Switzerland

*Corresponding author: luisa@eq.uc.pt

Keywords: Silica Aerogel Composite; Multi-walled Carbon Nanotubes; Graphene Oxide; Nano- and microstructure; Thermo-mechanical properties; Electrochemical behavior.

ABSTRACT: Carbon nanostructures-silica aerogel composites were synthesized and characterized to assess the effect of carbon nanotubes (CNTs) or graphene oxide (GO) on the silica aerogel properties. The sol-gel chemistry was based on methyltrimethoxysilane (MTMS) and 3-aminopropyltrimethoxysilane (APTMS) as silica precursor system, with varying amounts of APTMS (0-20 % mol of Si). APTMS significantly impacted the materials' physical properties. The chemistry and microstructure were investigated by FTIR, NMR, TEM, SEM, SAXS and BET: the addition of CNTs induced the growth of the silica matrix around them; thus, an elongated shape was observed in the silica structural units.

APTMS and CNTs have a synergistic effect on the mechanical properties, increasing the Young's modulus up to 14 MPa. Small amounts of carbon materials (~1 wt%) in the MTMS-matrix improved its thermal insulation property, particularly for temperatures above 50 ºC. In terms of electrochemical properties, the carbon nanostructures lead to higher specific capacitances and a reduction in resistance. The characterizations here performed allowed a better understanding of the interactions between the silica and carbon phases. The possibility to obtain materials with tailored properties demonstrates their application potential in several areas, such as thermal insulation and energy storage.

1. INTRODUCTION

Composites of carbon nanostructures with silica aerogels exhibit improved mechanical, electrical and thermal properties [1], which are affected by characteristics of the individual components, as well as the carbon material morphology and the interactions between their constituents. In addition to providing new and enhanced properties to silica aerogels, the presence of such nanomaterials usually does not have a significant impact in the silica aerogels unique properties like low density (0.03 to 0.3 $g.cm^{-3}$), high specific surface area (250 to 800 $m^2.g^{-1}$) and porosities higher than 90 %, with a combination of micro-, meso- and macroporosity [2].

Despite the interesting properties of carbon materials like high electrical conductivity and, especially, high mechanical strength [3, 4], the use of carbon nanotubes (CNTs) or graphene as additives of silica aerogels has just recently began to be exploited [1, 5–10]. Most of the research works in the literature focus on studying the effect of the carbon nanomaterials on the thermal conductivity and adsorption capacity of silica aerogels.

The majority of works where CNTs or GO are used lead to thermal conductivities between 16 and 67 $mW.m^{-1}.K^{-1}$ [6, 10–15]. However, thermal conductivity values as low as 7.2 $mW.m^{-1}.K^{-1}$ were achieved by Lei *et al*. [16], when 0.4 wt% of graphene oxide (GO) was added to tetraethylorthosilicate (TEOS)-based silica aerogels. However, this most likely is a strong underestimation since the determined thermal conductivity for the pure silica aerogel was also lower (8.9 $mW.m^{-1}.K^{-1}$) than the minimum values reported in the literature

(12 $mW.m^{-1}.K^{-1}$ [17] and 13 $mW.m^{-1}.K^{-1}$ [18]) for silica aerogels, at ambient pressure and temperature [19].

Regarding the adsorption capacity of aerogel composites with carbon nanomaterials, most of the studies focused on the adsorption of oils [20–23]. For diesel adsorption, multi-walled CNTs (MWCNTs)–silica aerogels developed by Huang *et al.* [20] showed an adsorption capacity of 28.48 $cm^3.g^{-1}$, indicating a synergistic effect between the MWCNTs and silica aerogel, since separately these materials showed adsorption capacities of 19.2 and 9.70 $cm^3.g^{-1}$, respectively. Improved adsorption capacity was also achieved by Loche *et al*. [22] for the removal of mineral oil through the addition of 0.1 wt% of graphene to silica aerogel, increasing the adsorption capacity by more than 20 %, when compared to that of the reference SiO_2 aerogel.

The addition of carbon nanomaterials also impacts the mechanical properties of silica aerogels, as reported by Piñero *et al*. [9] and Hong-li *et al*. [6]. By adding only 0.5 wt% of CNTs into a TEOS-based silica matrix, Piñero *et al*. [9] were able to significantly improve the mechanical parameters, with the composite achieving a compressive strength of 0.9 MPa and a maximum deformation of 74 %, while the pure silica aerogel collapsed upon 0.2 MPa stress and withstood less than 50 % deformation. In the work developed by Hong-li *et al*. [6] the mechanical strength was also enhanced by the insertion of GO into TEOS-based silica aerogels, changing from 0.04 MPa to 0.65 MPa with the increasing of GO content, from 0 wt% to 3 wt%.

Besides the previously mentioned properties, Meng *et al*. [24] reported an improvement in the electrochemical performance for an amorphous SiO_2@graphene aerogel (SiO_2@GA) composite. Even though the graphene aerogel showed superior specific charge capacity and cycling performance at low current densities than those of the composite, the SiO_2@GA exhibited better results at high current densities. The composite demonstrated high specific capacity, great cyclic stability and good rate capability, attributed to the aerogel three-dimensional structure and the graphene aerogel doping, while maintaining large surface area (S_{BET} = 396.9 $m^2.g^{-1}$) and high pore volume (V_P = 0.67 $cm^3.g^{-1}$). Hence, the SiO_2@GA was considered a promising candidate to be used as anode material in lithium-ion batteries.

Enhancing the unique properties of silica aerogels, as well as providing different characteristics by modifying their structure with distinct compounds, greatly relies on the chemical and physical characterization and the understanding of their micro- and nanostructure [25]. Until now, most studies combining carbon nanostructures with silica aerogels were carried out for composites with TEOS or water-glass as silica precursors. To the best of our knowledge, and except for our group's work [10], research using methyltrimethoxysilane (MTMS) for developing carbon nanostructures-silica aerogel composites has not been reported, despite the evident importance of MTMS as a precursor for silica aerogels and foams [26–31]. Moreover, comparison studies of the impact of different carbon nanostructures in the same silica aerogel system are yet to be performed. Hence, the goal of this work is to provide better understanding on the effect of 1D (carbon nanotubes) and 2D (graphene oxide) carbon nanomaterials on the chemical, physical and structural properties of MTMS-based silica aerogels, and enabling a direct comparison of their influence in the final aerogel characteristics, particularly in their fine chemical structure, thermo-mechanical properties and electrochemical performance. The addition of APTMS was also tested as co-precursor in small amounts, in order to decrease the gelation time and avoid settling of the carbon phase. This parameter significantly influenced the silica network features, and its study is equally an important contribution of this study to the progress of the state-of-the-art of organically-modified silica aerogels.

2. EXPERIMENTAL SECTION

2.1. Materials

Methyltrimethoxysilane (MTMS; purity ≥ 98 %, *Aldrich*; $CH_3Si(OCH_3)_3$), (3-aminopropyl)trimethoxysilane (APTMS; purity ≥ 97 %, *Aldrich*; $H_2N(CH_2)_3Si(OCH_3)_3$), ethanol (absolute, *Fluka*; C_2H_5OH), oxalic acid anhydrous (purity ≥ 99 %, *Fluka*; $C_2H_2O_4$), ammonium hydroxide (25 % NH_3 in H_2O, *Fluka Analytical*; NH_4OH), hexadecyltrimethylammonium bromide (CTAB; purity ≥ 99 %, *Sigma*; $C_{19}H_{42}BrN$), poly(ethylene glycol) 600 (PEG; purity ≥ 99 %, *Sigma*; $H(OCH_2CH_2)_nOH$), commercial multi-walled carbon nanotubes (CNTs; purity 90 %, *Nanocyl*, average diameter of 9.5 nm, average length of 1.5 µm, surface area of 250–300 $m^2.g^{-1}$), graphene oxide (GO; *Graphenea*,

concentration 0.4 wt%, monolayer content (at 0.05 wt%) ≥ 95 %), nitric acid (purity 70 %, *Sigma Aldrich*; HNO_3) and tetramethyl orthosilicate (TMOS; purity ≥ 99 %, *Aldrich*; $Si(OCH_3)_4$) were used in this work. Graphite powder (*Sigma–Aldrich*), mineral oil (*Sigma–Aldrich*), iron(III) chloride hexahydrate (purity 97 %, *Sigma Aldrich*, $FeCl_3.6H_2O$), potassium hydroxide (*Merck*, KOH) and ultra-pure water were also used. All reagents were used without prior purification.

2.2. Surface modification of carbon nanotubes

The multi-walled carbon nanotubes were submitted to two different surface modifications, as described in a previous work [10]. Briefly, MWCNTs were refluxed with concentrated HNO_3 for 20 hours at 50 °C, followed by filtering and washing with distilled water, then dried at 60 °C overnight. These MWCNTs were designated as CNTs-HNO_3. In the second surface modification protocol, the CNTs-HNO_3 were submitted to a reflux with a 10 % silane solution (TMOS in a mixture of 70 % ethanol/30 % water) for 4 hours at 70 °C, then filtered and dried at 60 °C for 1 day; these carbon nanotubes were denominated as CNTs-TMOS.

2.3. Synthesis of carbon nanomaterial-silica aerogel composites

The composite materials were prepared by a two-step acid–base catalyzed sol–gel process with oxalic acid (0.01 M in water) as acid catalyst, ammonium hydroxide (1 M in water) as basic catalyst and ethanol-water as the solvent. The samples were prepared with different proportions of silica precursors (MTMS, as main precursor and APTMS, as co-precursor). The synthesized silica aerogels are denoted as xMyA, where x in xM is the mol percentage of Si from MTMS, y in yA corresponds to the mol percentage of Si from APTMS. For the composites with CNTs (1D composites) and graphene oxide (GO) (2D composites), the designations xMyA_CNT_z and xMyA_GO_z were applied, respectively, where z is the amount in mg of carbon nanomaterial added to the system.

The use of surfactants was considered from the onset of this work to promote the dispersion of the carbon nanostructures in the silica sol. For the carbon nanotubes-silica aerogel composites, CTAB was the selected surfactant, as it ensures a good dispersion of the CNTs even in basic conditions [32]. The same surfactant was tested for the GO-silica aerogel

composites, however, when CTAB was added in the solution containing ethanol-water solvent and GO, a phase separation was observed (Figure S1). Thus, it was not possible to effectively disperse GO with CTAB. It was also tried to obtain the GO-silica aerogel composites without surfactant. Even though monolithic samples were achieved, SEM images showed that in this case, the GO was not evenly distributed in the samples, agglomerating in some parts of the silica matrix (Figure S2). So, it was necessary to use a different type of surfactant, PEG, for the GO composite samples, in order to obtain materials with better distribution of the carbon nanomaterial in the silica matrix.

The synthesis process started with the addition of a surfactant, CTAB for the CNTs samples and PEG for the GO samples (~4.0 wt% of the sol), into the solvent mixture (ethanol:water 50 %/50 % v/v), along with MTMS, followed by the addition of the acid catalyst. For the CNTs-silica aerogel composites, the suspension was sonicated for 30 minutes before MTMS addition. For the GO-silica aerogel composites, the suspension was stirred for 5 min before MTMS addition. After 30 minutes of the optional stirring, APTMS was added to the solution, followed by the ammonium hydroxide. The synthesis procedure was performed under thermal control at 27 ºC, gelation occurred within 15 minutes and the samples were aged for 7 days, at 27 ºC. Surfactant removal was carried out by diffusional ethanol washing, performing 8 changes, while the samples were kept in an oven at 60 ºC. The aerogel composites were dried at ambient pressure at 60 ºC, for 3 days and then at 100 ºC, for 3 hours.

Different quantities of carbon nanomaterials were added to the composites: up to 200 mg for carbon nanotubes (~0.6 wt% of the sol) and up to 100 mg for graphene oxide (~0.3 wt% of the sol). For the composites containing CNTs, it was possible to obtain monolithic samples with higher amounts of carbon nanomaterial (400 mg), but they could not be dispersed homogeneously in the ethanol/water solvent mixture, leading to the formation of large aggregates of CNTs. For the GO composites it was not possible to obtain materials using only MTMS, since these samples did not become a gel, remaining completely liquid even after one-week.

2.4. Characterization of the aerogel composites

As the main goal of this study is to compare the influence of 1D and 2D carbon nanomaterials in the silica aerogel matrix, several characterization techniques were employed to provide better understanding of the synthesized 1D and 2D carbon nanostructures containing silica aerogel composites.

2.4.1. Chemical characterization

Detailed information regarding the chemical structure of the aerogels network was obtained from Fourier Transform (FT) Infrared (IR) transmission spectroscopy. For FTIR analysis, a *Jasco FTIR 4200* equipment was used, recording a total of 256 scans from 4000 to 400 cm^{-1} with a resolution of 4 cm^{-1}. The spectra were collected using the potassium bromide (KBr) pellet method, the pellets being prepared with 78-80 mg of KBr and 0.2–0.3 mg of each aerogel. FT-Raman spectra were acquired with a *Horiba Jobin-Yvon LabRAM HR-UV 800*, micro-FT Raman spectrometer, using a laser excitation of 442 nm. The measurements were performed in the wavenumber range between 100 and 3000 cm^{-1}, exposure times of 20 seconds and up to 10 accumulations.

Solid-state nuclear magnetic resonance (SS-NMR) analysis was performed to assess the surface chemistry of the synthesized materials and to verify possible changes in the silica matrix caused by the addition of the 1D and 2D carbon nanomaterials. The spectra were collected as previously described by Malfait *et al*. [33, 34]. In summary, spectra were acquired with magic angle spinning (MAS) on a *Bruker* spectrometer equipped with a wide-bore 9.4 T magnet, corresponding to Larmor frequencies of 400.2 MHz for ^{1}H, 100.6 MHz for ^{13}C, and 79.5 MHz for ^{29}Si. To increase sensitivity, ^{1}H–^{13}C and ^{1}H–^{29}Si cross-polarization (CP) spectra were collected with 7 mm zirconia rotors, a spinning rate of 4500 Hz ± 2 Hz, and contact times of 2000 and 5000 µs, respectively. The spectra were acquired with a recycle delay of 2 s, *i.e*. between 1.3 and 4 times the ^{1}H T1 relaxation times typically observed for silica aerogels (0.5 to 1.5 s). The samples were ground and compressed before analysis and the zirconia rotors were filled completely to maximize sensitivity. The chemical shifts are relative to tetramethylsilane using adamantane and Si rubber as secondary chemical shift standards.

2.4.2. Structural characterization

The crystalline structure of the samples was evaluated using powder X-ray diffraction (*XRD Philips X'PERT-PRO* Diffractometer system), by collecting information in the range 2-70º (2θ) with step size of 0.02º, at room temperature, using CuKα radiation (λ = 1.54 Å) and operated at 40 kV/50 mA.

Bulk density (ρ_b) was determined by measuring and weighing the monolithic aerogels/composites, and the aerogel skeletal density (ρ_s) was measured by Helium pycnometry (*Accupyc 1330*, *Micromeritics*). The specific surface area (S_{BET}) was assessed by nitrogen gas adsorption at 77 K (*Gemini V2.00, Micromeritics Instrument Corp.*), applying the Brunauer-Emmett-Teller (BET) theory in the relative pressure interval 0.05–0.25 of the adsorption isotherm.

The porosity (equation 1) and pore volume (equation 2) were calculated using bulk and skeletal densities. The average pore size was estimated using the obtained values for pore volume and specific surface area (equation 3).

$$\text{Porosity (\%)} = (1 - \rho_b / \rho_s) \times 100 \quad (1)$$

$$V_P = (1/\rho_b) - (1/\rho_s) \quad (2)$$

$$\text{Average pore diameter} = 4(V_P)/S_{BET} \quad (3)$$

The morphology and microstructure of the developed materials was assessed by scanning electron microscopy (SEM; *Hitachi, SU-70*), operated at 15 kV, and scanning/transmission electron microscopy (STEM; *STEM Hitachi 2700* and *TEM JEOL, 2200FS*), operated at 200 kV. For SEM, powders were dropped directly onto a double-sided carbon tape. The material excess was removed under gentile nitrogen gas flow, and a conductive carbon thin film was deposited onto the specimens using a carbon rod coater (*Emitech K950X*). For TEM, the samples were dispersed in ethanol *p.a.*, manually shaken for a few minutes, being a drop of this dispersion placed onto a 400 mesh copper grid with a continuous carbon film and left to dry in air. High-resolution (HR) TEM images were processed using the software *Digital Micrograph 3.42*.

Small angle X-ray scattering (SAXS) was used to provide insight of the materials at the nanoscale, obtain information about primary and secondary silica particles, and study the influence of carbon nanomaterials' addition on the nanopores formation. The SAXS analysis

was performed using a *NanoStar* instrument (*Bruker AXS GmbH,* Karlsruhe, Germany). The instrument was equipped with a micro focused X-ray source (*Incoatec GmbH,* Geesthacht, Germany), with a beam spot size of about 400 µm and Cu *Kα* radiation (λ = 0.154 nm). The scattering intensities from both background and samples were acquired for 60 s at 107 cm detector distance. A *VÅNTEC-2000* Xe-based gas avalanche detector with 2048x2048 pixels and the pixel size of 68x68 µm was used. The minimum reliably measured scattering vector magnitude, q_{min}, is 0.1 nm^{-1}, with $q = (4\pi/\lambda) \sin \theta$, where 2θ is the scattering angle. All experiments were carried out under vacuum (~ 0.01 mbar) to minimize the background scattering from air. Powder samples were used for the measurements, with the samples being placed in a holder and secured with Kapton film. The background scattering from Kapton was subtracted from the experimental data prior to the data analysis.

2.4.3. Thermo-mechanical characterization

Thermal conductivity was assessed by the transient plane source (TPS) technique, at 20 ºC (*Thermal Constants Analyzer TPS 2500S, Hot Disk*). For selected samples, this analysis was also carried out at different temperatures within the range of -25 ºC to 175 ºC. Thermal gravimetric analysis (TGA, *TGA-Q500*, *TA Instruments*) was used to determinate the maximum service temperature allowed for the synthesized materials. The analyses were performed from room temperature to 600 °C, with a heating rate of 10 °C.min^{-1}, under nitrogen flow. For mechanical evaluation, uniaxial compression-decompression tests, on samples with approximately 15 x 15 x 10 mm^3, were run using a load cell of 50 N, up to 10 % strain at a deformation rate of 0.5 mm.min^{-1} [35, 36], and then back to residual strain by removing the load at the same speed. The Young´s modulus was obtained from the initial linear region of the loading curve and the energy loss coefficient was determined using equation (4) [37]:

$$\text{Energy loss coefficient (\%)} = \frac{\text{Area under loading curve} - \text{Area under unloading curve}}{\text{Area under loading curve}} \text{ x } 100 \qquad (4)$$

2.4.4. Electrochemical characterization

Potentiodynamic electrochemical cyclic voltammetry (CV) and electrochemical impedance spectroscopy (EIS) measurements were performed by using a *PalmSens* portable potentiostat/galvanostat, *PalmSens4*, integrating an EIS analyzer module. This device was controlled by the *PSTrace 5.5* software (*PalmSens*, Netherlands). The cyclic voltammograms were recorded within the potential range of -0.5 to 0.2 V and scan rates from 5 up to 400 $mV.s^{-1}$. EIS measurements were performed at an open circuit potential, using a sinusoidal wave with an amplitude of 0.01 V and 73 data points logarithmically distributed over 0.01 –10000.0 Hz frequency range. A modified carbon paste electrode was the working electrode, a Pt wire the counter electrode and Ag/AgCl the reference electrode. The carbon paste (100 mg) electrode was prepared by carefully mixing graphite powder (50 % (w/w)) with aerogel samples (25 % (w/w)) and subsequently adding mineral oil (25 % (w/w)). The components were mixed manually in a mortar until complete homogenization. The obtained material was packed into an adequate support of electrode consisting of a cylindrical plastic tube (internal diameter 5 mm) with a copper rod inside used as an external electric contact [38]. The electrochemical experiments were carried out in a KOH 6M solution, using a three-electrode system in one-compartment electrochemical cell of 5 mL capacity at 25 ºC.

The specific capacitances obtained from the CV were calculated by equation (5) [39–41].

$$C_S = (\int I\mathrm{d}V)/(2\ (\upsilon\ m\ \Delta V)) \quad (5)$$

where C_S is the specific capacitance, $\int I\mathrm{d}V$ represents the area under voltammetric curve, υ is the scan rate, m is the mass of aerogels used in the working electrode and ΔV is the potential window.

3 RESULTS AND DISCUSSION

3.1 Chemical characterization

FTIR analysis showed that the presence of carbon nanomaterials was not detected in the spectra, even when higher amounts were used in the samples, with only the typical silica bands being identified. These findings were expected, as previously observed for carbon

nanotubes-silica aerogel composites [10]. In both examples of FTIR spectra shown in Figure 1a, bonding between silicon and oxygen is observed, indicating that the precursors have originated a silica network. The symmetric stretching vibrations of the Si–O–Si bonds, the Si–C stretching vibration from the methyl group of MTMS and the bands associated to the longitudinal and transversal-optical components of the asymmetric stretching vibration of Si–O–Si appear around 760 cm^{-1}, 835 cm^{-1}, 1040 cm^{-1} and 1140 cm^{-1}, respectively [42]. Regarding the use of different surfactants, such as PEG or CTAB, both composites aerogels present similar silica bands, indicating that the use of these different compounds in the synthesis does not have a major effect on the chemical structure of the silica network.

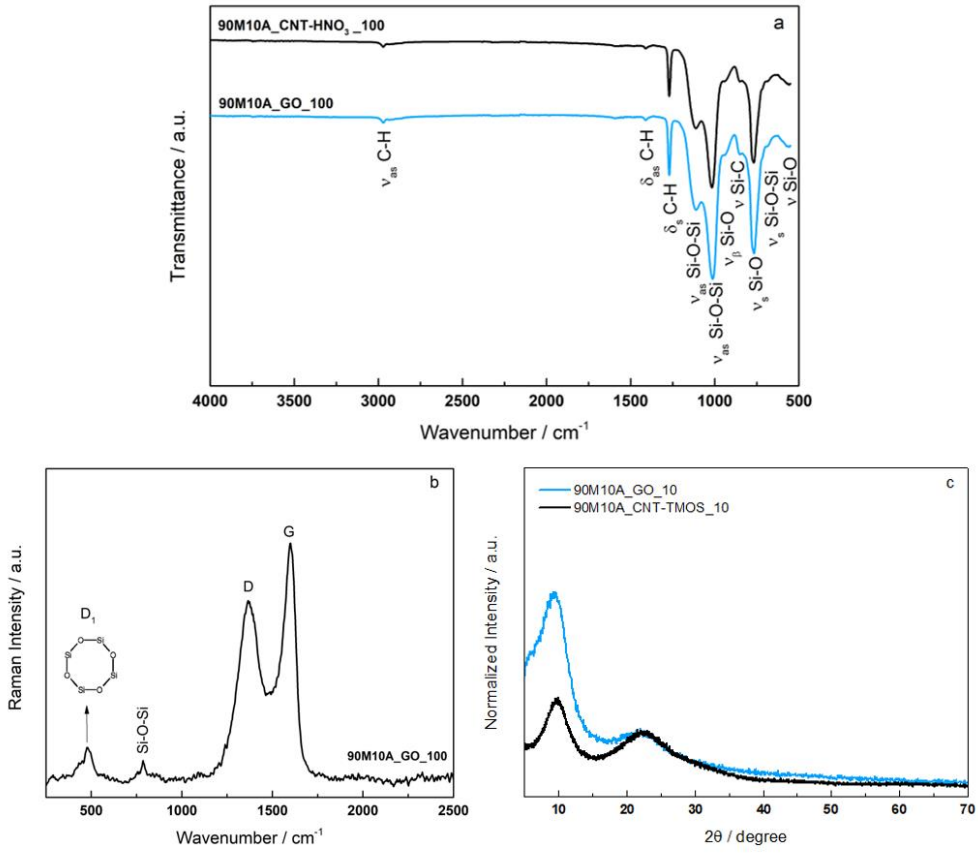

Figure 1. Chemical and structural characterizations of carbon nanomaterials-silica aerogel composites: a) FTIR spectra, b) Raman spectra and c) powder X-ray diffraction patterns (normalized). (For color, refer to the online version).

The presence of carbon nanomaterials in the composites was then confirmed by Raman spectroscopy. The spectra for the aerogels synthesized with both 1D and 2D nanomaterials, carbon nanotubes [10] and graphene oxide (Figure 1b), exhibit the two characteristic absorption bands, D band (around 1350 cm^{-1}) and G band. For the GO composite, the G band is at approximately 1597 cm^{-1}, which agrees with the literature for GO with high levels of oxidation [43–45]. A broad signal near 500 cm^{-1}, assigned to Si-O-Si bending vibrations and rings with 4 -Si-O- units (D1) [46–52], and a signal near 790 cm^{-1}, also assigned to Si-O-Si vibrations, are observed in all composites, independent of the presence or concentration of 1D and 2D carbon nanostructures.

The effect of APTMS addition into the MTMS-based silica aerogel was studied by solid-state MAS NMR, as illustrated in Figure 2. The ^{29}Si spectra (Figure 2a) display the T^n resonances arising from Si atoms originating from the hydrolysis and condensation of MTMS and APTMS, with T^3 corresponding to Si atoms with one carbon neighbor and three bridging oxygen atoms (BO) and T^2 to Si atoms with one carbon neighbor, two BO and one non-bridging oxygen (NBO) atom [53]. The ^{29}Si spectra are very similar for all aerogels, with the T^2 band (-58 ppm) accounting for only around 10 % of the T^3 (-67 ppm) intensity [53], indicating a high degree of condensation of the trifunctional silane during aerogel synthesis.

More significant differences between the samples were observed in the ^{13}C spectra (Figure 2b). When APTMS is added to the MTMS based aerogels, the carbons from aminopropyl chains are clearly visible in the spectra (at 11, 27 and 45 ppm with increasing distance from the amino group), and their intensity scales with the APTMS content used during synthesis. The position and width of the main Si-CH_3 signal at -3 ppm remain unchanged upon APTMS addition.

The influence of the use of different surfactants (CTAB and PEG) in the synthesis process on the final chemical structure of the silica aerogels was also assessed. The ^{1}H–^{29}Si CP MAS NMR spectra are near-identical when using PEG versus CTAB (Figure S3a). Even though the ^{1}H–^{13}C CP MAS NMR spectra are also quite similar, a small additional peak around 73 ppm is observed for the sample synthesized with PEG, indicating the retention of a residual amount of PEG in the system (Figure 2c). It is possible that the retention of this surfactant is caused by the hydrogen bond interactions between the oxygen atoms and

terminal OH groups of PEG with the amino groups of the APTMS precursor or residual silanol groups in the silica network. Alternatively, some PEG may be possibly covalently bonded to the silica network through alcoholysis between the PEG terminal OH and residual silanol. Due to these strong interactions, it was evidently not possible to completely remove PEG from the system using only diffusional washing, although the presence of this surfactant is minor based on its low NMR intensity. It does not affect the chemical structure of the silica network, as confirmed by the already mentioned similarity of the ^{1}H–^{29}Si CP MAS NMR spectra.

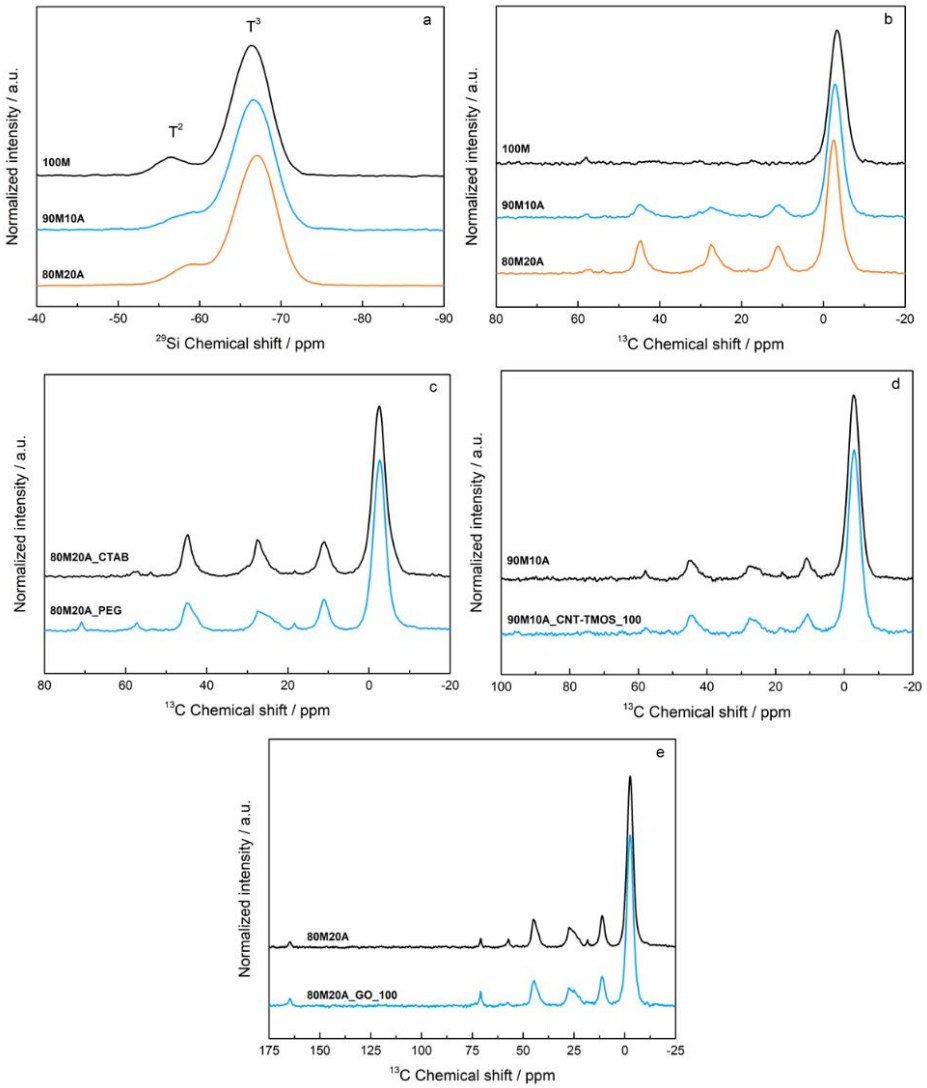

Figure 2. a) ^{1}H–^{29}Si solid-state MAS NMR spectra of MTMS based aerogels synthesized with variable APTMS content (0, 10 and 20 % of total Si atoms from top to bottom); b) ^{1}H–^{13}C solid-state MAS NMR spectra of

MTMS based aerogels synthesized with variable APTMS content (0, 10 and 20 % of total Si atoms from top to bottom); c) $^{1}H–^{13}C$ solid-state MAS NMR spectra of 80 % MTMS/20 % APTMS silica aerogels synthesized with CTAB versus PEG as surfactant; d) $^{1}H–^{13}C$ solid-state MAS NMR spectra of 90 % MTMS/10 % APTMS silica aerogels synthesized with and without CNTs; and e) $^{1}H–^{13}C$ solid-state MAS NMR spectra of 80 % MTMS/20 % APTMS silica aerogels synthesized with and without GO. (For color, refer to the online version).

The presence of carbon nanotubes has only minor effects on the $^{1}H–^{29}Si$ CP MAS NMR (Figure S3b) and $^{1}H–^{13}C$ CP MAS NMR spectra (Figure 2d). The ^{29}Si spectra are nearly identical, indicating no major chemical changes in Si-O-Si condensation with or without carbon nanotubes, even though some differences between them are observed by the structure-based analytical techniques such as TEM, SEM, SAXS and BET (see below). A direct detection of the used carbon nanomaterials with $^{1}H–^{13}C$ CP MAS NMR is not possible due to the low loading of these materials and relatively low sensitivity of SS-NMR. When graphene oxide was added into the silica matrix, some small differences could be observed: a broadening of the main CH_3 peak (-2.6 ppm), as well as an intensity decrease and slight broadening of the APTMS peaks (Figure 2e). These differences indicate that more variations in the local environment around the methyl and aminopropyl groups occur in the presence of the GO sheets.

Therefore, solid state MAS NMR results demonstrate that both 1D and 2D carbon nanomaterials do not prevent or significantly affect the condensation of the silica precursors into the three-dimensional network. However, the presence of carbon nanostructures with two dimensions (2D), in this case graphene oxide, has a small, but measurable impact on the local chemical environment of the organic groups.

3.2 Structural characterization

Powder X-ray diffraction patterns were obtained for the 1D and 2D carbon structures-silica aerogel composites (Figure 1c). The broad XRD patterns indicate the amorphous nature of the materials. Two broad reflections are observed for both the GO and CNT composite samples. These peaks are typical for sol-gel derived materials from MTMS [54] and have been previously reported for 1D carbon nanotubes-silica aerogel composites [10]. The bands can be attributed to the d-spacing between silicon atoms linked to alkyl groups (methyl or propyl) (around 9°) and to those of the Si-O-Si network, similar to silica glass (around 22°)

[10, 54, 55]. As presented in Figure 1c, in the normalized patterns, the band around 9° for the GO-containing composites has higher relative intensity than the CNTs-containing composites. A possible explanation is the fact that GO has a typical reflection in this region assigned to the interlayer d-spacing around 0.87 nm [43, 56–61], but it is unlikely that the relatively low amount of GO can account for the large difference.

The physical and microstructural properties of the reference silica aerogels and their corresponding 1D and 2D carbon-containing composites are summarized in Tables 1 and 2.

Table 1: Physical and microstructural properties of the reference silica aerogels and CNTs-silica aerogel composites (CTAB as surfactant).

Samples	Bulk density ($kg.m^{-3}$)	Porosity (%)	Pore volume ($cm^3.g^{-1}$)	Specific surface area ($m^2.g^{-1}$)	Average pore size (nm)
100M [10]	75.3 ± 5.1	95.3 ± 0.1	12.6 ± 0.9	458.1 ± 2.2	110.5 ± 6.9
100M_CNT-HNO_3_10	72.8 ± 3.9	94.6 ± 0.1	13.0 ± 0.7	477.7 ± 1.7	108.8 ± 6.2
100M_CNT-HNO_3_50	90.7 ± 8.2	94.7 ± 0.1	10.4 ± 0.5	438.5 ± 2.4	95.2 ± 5.4
100M_CNT-HNO_3_100	92.1 ± 4.9	94.6 ± 0.1	10.3 ± 0.6	485.1 ± 2.6	84.7 ± 4.9
100M_CNT-HNO_3_200	96.6 ± 7.7	94.3 ± 0.2	9.8 ± 0.1	463.0 ± 2.5	84.4 ± 1.5
100M_CNT-TMOS_10 [10]	75.6 ± 5.1	95.6 ± 0.2	12.7 ± 1.4	492.4 ± 4.0	102.7 ± 10.3
100M_CNT-TMOS_50	65.4 ± 4.0	96.1 ± 0.1	14.7 ± 0.9	422.2 ± 6.8	139.3 ± 10.8
100M_CNT-TMOS_100	77.8 ± 1.6	95.4 ± 0.2	12.3 ± 0.2	486.3 ± 2.1	100.9 ± 2.4
100M_CNT-TMOS_200	82.9 ± 2.4	95.1 ± 0.1	11.5 ± 0.3	430.6 ± 7.3	106.5 ± 4.7
90M10A [10]	80.9 ± 7.2	94.5 ± 0.3	11.7 ± 1.0	72.2 ± 1.3	647.4 ± 46.1
90M10A_CNT-HNO_3_10	81.9 ± 4.3	93.2 ± 0.2	11.4 ± 0.6	306.9 ± 4.3	148.4 ± 9.6
90M10A_CNT-HNO_3_50	95.6 ± 6.7	93.8 ± 0.1	9.8 ± 0.7	131.1 ± 1.6	299.6 ± 25.0
90M10A_CNT-HNO_3_100	92.1 ± 7.6	94.1 ± 0.2	10.2 ± 0.9	134.9 ± 1.7	303.0 ± 29.4
90M10A_CNT-HNO_3_200	101.4 ± 7.3	93.5 ± 0.1	9.2 ± 0.7	90.8 ± 2.5	406.2 ± 41.5
90M10A_CNT-TMOS_10 [10]	84.6 ± 5.1	94.6 ± 0.1	11.2 ± 0.7	118.2 ± 2.1	387.3 ± 15.6
90M10A_CNT-TMOS_50	81.9 ± 5.1	94.8 ± 0.2	11.6 ± 0.4	79.1 ± 1.1	669.7 ± 33.8
90M10A_CNT-TMOS_100	86.9 ± 2.8	94.4 ± 0.1	10.9 ± 0.5	54.3 ± 0.8	800.5 ± 46.5
90M10A_CNT-TMOS_200	83.1 ± 4.8	94.7 ± 0.1	11.4 ± 0.7	115.9 ± 2.4	393.2 ± 31.0
80M20A [10]	381.7 ± 24.2	72.3 ± 1.6	1.9 ± 0.2	311.9 ± 7.7	24.3 ± 1.5
80M20A_CNT-HNO_3_10	474.6 ± 21.3	66.5 ± 0.8	1.4 ± 0.1	268.1 ± 5.2	20.9 ± 1.6
80M20A_CNT-HNO_3_50	381.1 ± 13.8	73.1 ± 0.4	1.9 ± 0.1	132.2 ± 1.7	58.1 ± 3.2
80M20A_CNT-HNO_3_100	437.7 ± 9.5	69.1 ± 0.1	1.6 ± 0.1	180.8 ± 2.4	34.9 ± 1.3
80M20A_CNT-HNO_3_200	427.4 ± 4.8	69.8 ± 0.1	1.6 ± 0.1	208.9 ± 2.7	31.3 ± 1.2
80M20A_CNT-TMOS_10 [10]	142.2 ± 0.5	89.9 ± 0.2	6.3 ± 0.1	245.6 ± 3.2	103.0 ± 0.8
80M20A_CNT-TMOS_50	386.4 ± 5.8	72.7 ± 0.1	1.9 ± 0.1	175.3 ± 2.4	43.0 ± 1.2
80M20A_CNT-TMOS_100	355.3 ± 1.1	74.9 ± 0.4	2.1 ± 0.1	313.1 ± 4.3	26.9 ± 0.3
80M20A_CNT-TMOS_200	305.1 ± 11.1	78.5 ± 0.4	2.6 ± 0.1	340.5 ± 3.8	30.2 ± 1.6

Table 2: Physical and microstructural properties of the reference silica aerogels and GO-silica aerogel composites (PEG as surfactant).

Samples	Bulk density ($kg.m^{-3}$)	Porosity (%)	Pore volume ($cm^3.g^{-1}$)	Specific surface area ($m^2.g^{-1}$)	Average pore size (μm)
90M10A	88.4 ± 3.0	93.7 ± 0.1	10.6 ± 0.4	9.4 ± 0.4	4.5 ± 0.2
90M10A_GO_10	82.9 ± 4.2	94.1 ± 0.2	11.4 ± 0.6	5.5 ± 0.5	8.3 ± 0.7
90M10A_GO_50	80.4 ± 3.3	94.3 ± 0.2	11.7 ± 0.5	25.8 ± 1.1	1.8 ± 0.1
90M10A_GO_100	86.8 ± 3.4	93.8 ± 0.2	10.8 ± 0.4	34.3 ± 1.2	1.3 ± 0.1
80M20A	79.2 ± 5.1	94.6 ± 0.1	11.9 ± 0.5	20.4 ± 0.5	2.3 ± 0.1
80M20A_GO_10	76.1 ± 2.6	94.8 ± 0.1	12.5 ± 0.4	22.4 ± 0.8	2.2 ± 0.1
80M20A_GO_50	73.8 ± 1.7	95.0 ± 0.2	12.9 ± 0.8	29.3 ± 0.9	1.7 ± 0.1
80M20A_GO_100	73.5 ± 2.8	95.0 ± 0.1	12.9 ± 0.3	71.9 ± 1.1	0.7 ± 0.1

The reference samples (without carbon nanostructures), independent of the surfactant type, have densities (75.3 to 88.4 $kg.m^{-3}$) similar to the ones obtained for other MTMS-based xerogels and aerogels in the literature [30, 62, 63], with the exception of the material containing 20 % of APTMS synthesized with CTAB, that displays a higher value of bulk density (381.7 $kg.m^{-3}$). The high density for this particular sample is related to the significant shrinkage suffered by this material during the drying step.

Contrary to the bulk density, systematic variations in specific surface area are observed for the reference aerogels. The aerogels synthesized with CTAB as surfactant (Table 1), even for the higher density 20 % APTMS material, have higher surfaces areas than the aerogels produced with PEG as surfactant (Table 2). The difference in surface area reflects the distinct microstructures, as observed by SEM (Figure 3). The materials synthesized with CTAB have a finer microstructure, which leads to higher values of specific surface area, while the samples obtained with PEG have a coarser structure, with significant larger particles and pores, and, consequently, lower surface areas.

The increase of amine amount added in the MTMS system with CTAB as surfactant, first results in a significant reduction (with 10 % of APTMS), followed by an increase in the specific surface area (with 20 % of APTMS), but not fully reaching the value of the 100M system. These variations can be related to the different particle radii obtained for these networks, as also observed for the different surfactants. As expected, the addition of amine groups leads to an increase in the particle radii, since the silica growth is not limited by cluster hydrolysis under more basic conditions [10, 64, 65], and therefore, lower values of specific

surface area are obtained for the resultant material. However, for the sample with 20 % of APTMS and CTAB, a decrease in the secondary particles' diameters, associated with higher values of surface area, was observed. There are two possible explanations for this. First the higher amount of APTMS in the system can favor nucleation, so the silica particles growth is more distributed through the whole solution in a higher number of nuclei, leading to smaller particles. The second reason may be the combination of higher amounts of APTMS and CTAB, which causes higher steric barriers against particle aggregation, leading to the stabilization of smaller particles [64].

For the samples synthesized with PEG, it is likely that PEG is only assisting the dispersion of graphene oxide in the solution, but not effectively controlling/preventing silica particle growth. Similar large secondary particles were found in works where no surfactant was used and higher amounts of water were added into the system [66, 67]. The explanation for these larger particles is mainly related to the presence of excess water in the system without a surfactant that is able to control the silica growth. For H_2O/MTMS molar ratios higher than 8, the hydrolysis and condensation reactions can be complete due to the over-stoichiometric conditions, not limiting the particles growth [66]. Also, the increase of aqueous equivalents changes the solvent to an anti-solvent ratio, which causes the silica particles to grow more separately, leading to larger sizes and the presence of macropores [67]. Under these particular conditions, the microstructure of the synthesized materials shows larger pores and spherical shaped particles, as observed in the SEM images (Figure 3).

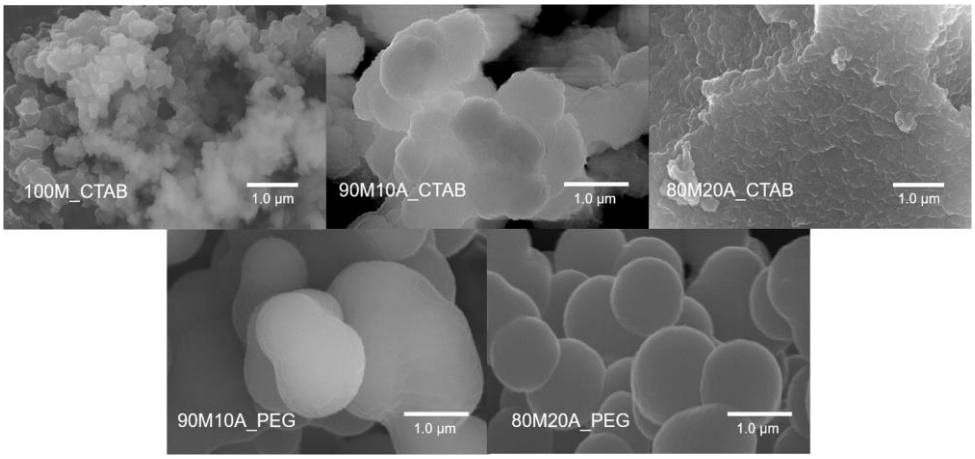

Figure 3. SEM images of the prepared silica aerogel with different surfactants (CTAB or PEG).

Regarding the composite materials, except for the samples with carbon nanotubes and 20 % of APTMS in the matrix, all materials show similar values for bulk density (65.4 to 101.4 $kg.m^{-3}$). Moreover, some samples presented even lower bulk density than those observed for MTMS xerogels and aerogels [30, 62, 63], or for carbon nanostructure-silica aerogel composites obtained with different precursors, dried under ambient pressure conditions [6, 20, 68–70].

For the 1D carbon-based composites, most of the samples synthesized with CNT-HNO_3 show higher values of bulk density than their counterparts prepared with CNT-TMOS, indicating that higher shrinkage occurs for these samples during the drying step. One possible explanation is that a better interaction between the silica matrix and the silane-modified carbon nanotubes is achieved, with these materials showing a better support to the silica skeleton than those only submitted to the acid surface modification. In general, for the composites 100M and 90M10A obtained with CNT-HNO_3, the increasing amount of carbon nanotubes increases the bulk density. Even though it was observed that the sample 90M10A_CNT-HNO_3_100 has a slightly lower value than the composite with 50 mg of CNT-HNO_3, this variation is within the range of experimental error, which supports the conclusion that the bulk density of these materials follows a nearly linear trend. For the same systems with CNT-TMOS, bulk densities are similar and do not show significant variations with the increase of carbon nanotubes in the samples. Regarding the 80M20A systems, much higher density values are obtained for the composites, similar to that of CNT free reference sample. Nevertheless, it is important to mention that when the added amount of CNTs was equal or higher than 50 mg, and regardless of their high-level shrinkages, the final composites remained monolithic, in contrast to what is observed for lower quantities of CNTs, independent of their surface modification. This indicates that when the carbon nanotubes start to connect to each other, they are able to sustain the silica matrix, avoiding the fracture of the final samples during drying.

For the 2D carbon-containing composites (shown in Table 2) no significant bulk density variations were noticed, including for the 80M20A, GO free reference sample, in contrast to the 80M20A reference sample from the CNT batch. Samples with higher amount of amine precursor show slightly lower values than those obtained with 10 % of APTMS, and the GO-

composites always have lower bulk density than their reference silica aerogel counterparts. A possible explanation for these results is that the presence of a carbon nanostructure, such as GO, with a significant different shape than the silica matrix may have some physical influence during the development of the 3D aerogel network. In the end, the 2D nanostructure helps to prevent the shrinkage of these composites even when prepared with higher quantity of APTMS.

In terms of porosity, again except for the samples synthesized with CNTs and 20 % of APTMS that result in values between 65 % and 90 %, the remaining matrices and composites present similar porosities, with values higher than 93 %. These porosity values are similar or even higher than those reported for MTMS-based aerogels dried with supercritical fluids [30, 71–73], or those for carbon nanostructures-silica aerogel composites [15, 20, 69, 74]. The pore volume is also very similar, although these materials present a large amount of macropores in their structure and the method is not sensitive enough to micro and mesopores variations.

Regarding the specific surface area, all samples synthesized only using MTMS as precursor show values consistent with those in the literature (420 - 500 $m^2.g^{-1}$). Aerogels usually present specific surface areas between 250 and 800 $m^2.g^{-1}$ [2], and some of our systems show even higher values than those reported for MTMS-based silica materials dried under similar conditions [30, 33]. Nonetheless, when amine groups are included in the structure, a decrease of the specific surface area is observed in all systems.

The presence of CNTs also influences the specific surface area, as observed for most of the 90M10A samples, whose CNTs-containing composites show higher values independently of the CNTs surface modification process. This is most probably due to stereological reasons, as CNTs provide points of nucleation for the silica growth, altering the network morphology [10], as observed in the SEM images (Figure 4). In contrast, for the 80M20A samples, most of the composites present lower values of specific surface area. A possible justification for these, is that, as mentioned for the 90M10A samples, the presence of CNTs favors the silica growth, which can lead to larger secondary particles than the reference sample.

The GO-based composites present lower values for specific surface area, if compared with the composites containing 1D carbon nanomaterial, which can be due to large particle radii,

in the micrometers order formed in the overall network, as confirmed by SEM imaging (Figure 5). Regarding the specific surface area values determined for the GO-added composites, the highest values are observed for those containing 100 mg of GO (~ 4 wt% of the aerogel), but these may have a contribution of the exposed GO high surface area, and not from the aerogel silica matrix itself.

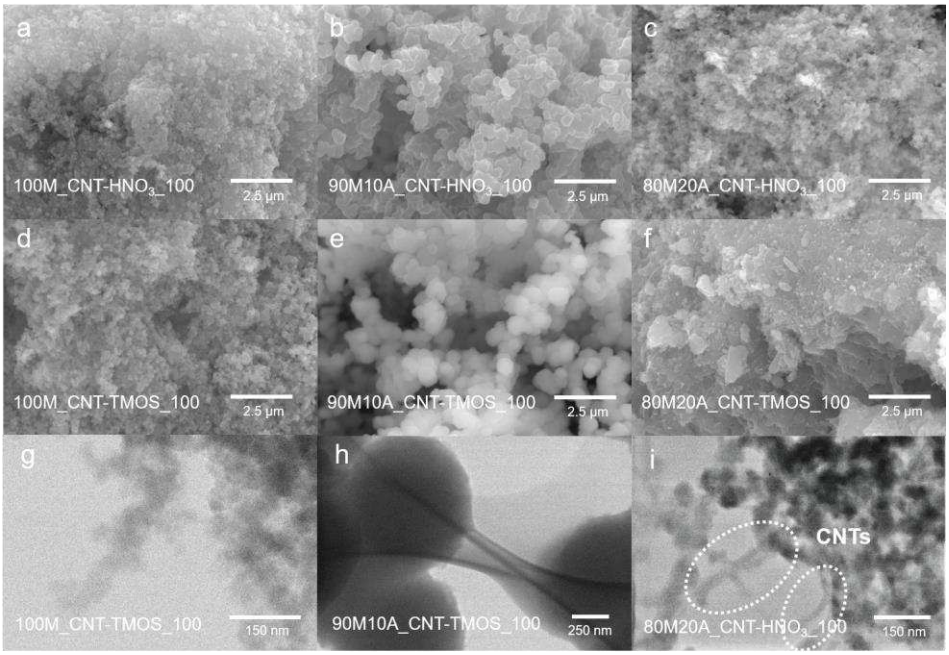

Figure 4. SEM (a to f) and TEM (g to i) images of the prepared carbon nanotubes-silica aerogel composites with 100 mg of the CNTs.

SEM images of the 1D and 2D carbon-containing composites (100 mg of carbon material) are shown in Figures 4 and 5, respectively. Generally, the images show the typical silica network morphology of secondary particles, also known as pearl-necklace-like structure [75]. It is also possible to observe that the samples with 90M10A and CNTs, and all the GO-added composites, present much larger pores and secondary particles than the remaining materials. The presence of such large particles is expected for the samples with APTMS as co-precursor [10, 64, 65], as mentioned for the reference samples. Another factor contributing to the growth of secondary particles is the fact that, during the washing steps, the aging process

continues to happen, which leads to the re-dissolution and re-precipitation of silica, resulting in the decrease of the specific surface area [76], which agrees with previous observations.

Moreover, the calculated average pore sizes in Tables 1 and 2 are also in good agreement with what is observed from SEM analysis. The influence of using carbon nanostructures with different surface treatments on the silica network formation was not detected by SEM imaging, since all samples present very similar silica matrices. Furthermore, due to the significant difference in size between the carbon nanostructures and the overall silica network, especially those presenting large secondary units, it was not possible to clearly distinguish the 1D/2D structures within the aerogel matrix. Thus, TEM analysis was performed to better assess the carbon nanostructures presence in such composites, as illustrated in Figures 4 and 5.

The microstructure of the CNT-silica composite aerogel synthesized with 100 % MTMS (Figure 4g) is composed of very small structural units, with the silica nanoparticles clearly decorating the interlinked carbon nanotubes. In the 90M10A_CNT-TMOS_100 composite (Figure 4h), the silica matrix evolved around the carbon nanotube, ending in a more elongated shape linked to the remaining network. The CNTs modification with a silane precursor most probably improves the chemical interaction between the two distinct materials, with the 1D nanostructure clearly connecting the silica clusters. In contrast to the CNTs-TMOS composites, where it was not possible to differentiate the two phases, the 80M20A_CNT-HNO_3_100 sample (Figure 4i) undoubtedly show a few disconnected carbon nanotubes. These observations were expected since the interaction between CNTs modified with nitric acid and the silica matrix is certainly weaker than that between silanized CNTs and the silica network.

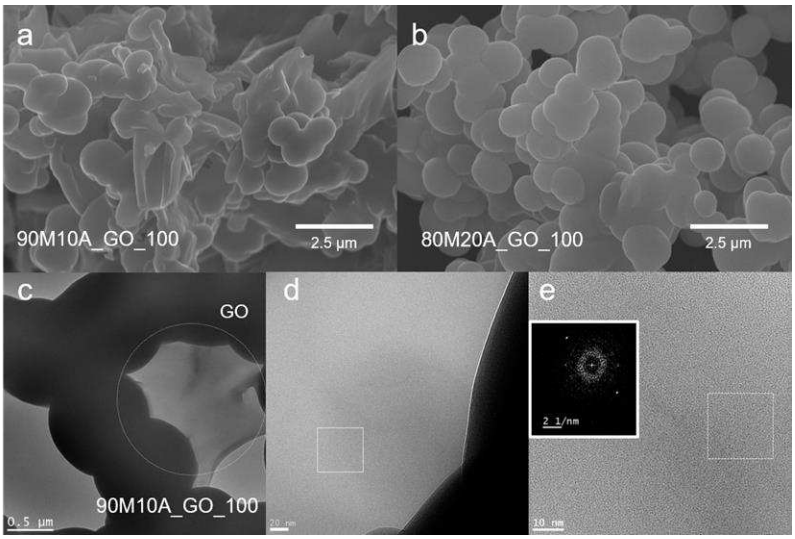

Figure 5. SEM images (a and b) and HRTEM images (c and d) of the prepared graphene oxide-silica aerogel composites with 100 mg of the GO and generated Fourier transform image (e).

Regarding the composites with GO, it is possible to observe a small part of the graphene oxide sheet next to the silica matrix (sample 90M10A_GO_100 - Figure 5c), with larger secondary silica particles as observed in the corresponding SEM image (Figure 5a). HRTEM imaging analysis mostly revealed single or a few layers GO involved within the silica framework. Nevertheless, detailed inspection also exposed a few areas where a small number of fragmented GO sheets have agglomerated. The generated Fourier transform diffraction pattern (inset of Figure 5e) shows a ring like pattern and spots typical of polycrystalline nature with crystallographic orientation between the sheets, respectively [45, 77]. Most of the graphene oxide identified in the aerogel matrix clearly shows diffraction spots for short-range order over a length scale, like those of graphite/graphite oxide [45]. These images illustrate the GO crystalline structure confirmed by the generated diffraction spots with a six-fold pattern [43, 45, 77]. HRTEM images also demonstrate the characteristic high transparency of the GO layer deposited onto the carbon film of the grid [45]. These findings are in very good agreement with those from powder XRD and Raman spectroscopy.

To investigate more in detail the morphology and porosity of the composite materials, SAXS measurements were performed on samples with and without carbon nanotubes (Figure S4). This technique was also performed in graphene oxide-silica aerogel composites, however, only a plateau was observed due to the large particle sizes of these samples, and an

ultra-small angle setup would be necessary. X-ray scattering patterns were analyzed to reveal two important structural features [78]. The first one is associated with the decay of scattering intensity at small angles, best explained by the classical Porod analysis. In this approach, the decay rate of scattering intensity follows $1/q^{\alpha}$ with α known as Porod exponent. For three-dimensional particles and perfectly smooth surfaces, a Porod exponent of 4 is expected. For particles with surface roughness, this exponent decreases to a minimal value of 3. The rougher the particle surface is, the smaller is the Porod exponent. We have analyzed the initial decay rate by the slope of scattering intensity versus q curve in log-log scale. The results are summarized in Figure 6.

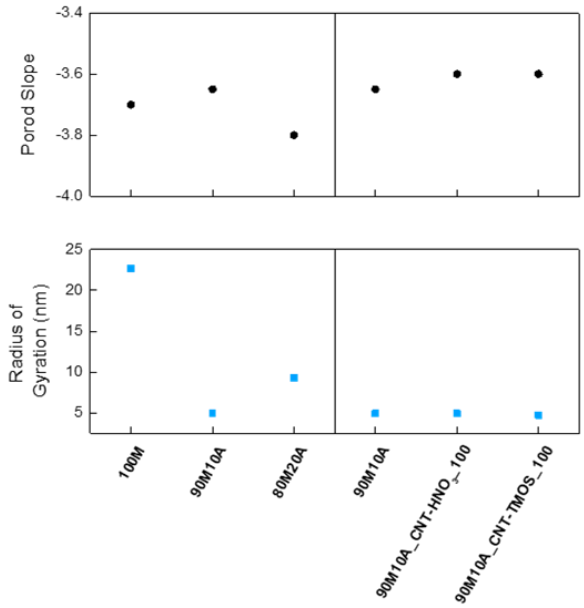

Figure 6. Porod slope values and radius of gyration (R_g) obtained from silica aerogels and carbon nanotubes-silica aerogel composites with 100 mg of CNTs.

The comparison of Porod slope values for three different matrices indicates only small variations around -3.72 ± 0.06, with the sample 90M10A displaying highest surface roughness (lowest Porod exponent). The addition of carbon nanotubes caused an increase in the Porod exponent (reduction of absolute values), so that both CNTs-silica aerogel composites studied (Figure 6) show a Porod exponent of -3.6. This variation confirms the fact that CNTs effectively modify the formation of the silica network, *i.e.* the microstructure

of the aerogels, and this higher surface roughness demonstrates a good agreement with the morphology observed in TEM images (Figure 4).

The second feature obtained from scattering curves is associated to nanometer-sized pores within the silica particles. This appears as a broad hump at larger scattering angles, *e.g*. shown in Figure 7 at the q values between 0.5 and 1.0 nm^{-1}. The position and intensity of this hump explains the size and the number density of pores. To acquire a quantitative measure of these pores, the previously obtained Porod decay function was subtracted from the experimental data and the resulting curve is interpreted as the scattering signal from internal pores. Further analysis of the deduced curves by indirect Fourier transformation [79] leads to the identification of a pair-distance distribution function (PDDF) and the average radius of gyration of pores. Similar approaches have been applied previously to reveal the pore size and surface roughness of the silica particles from SAXS data [78, 80].

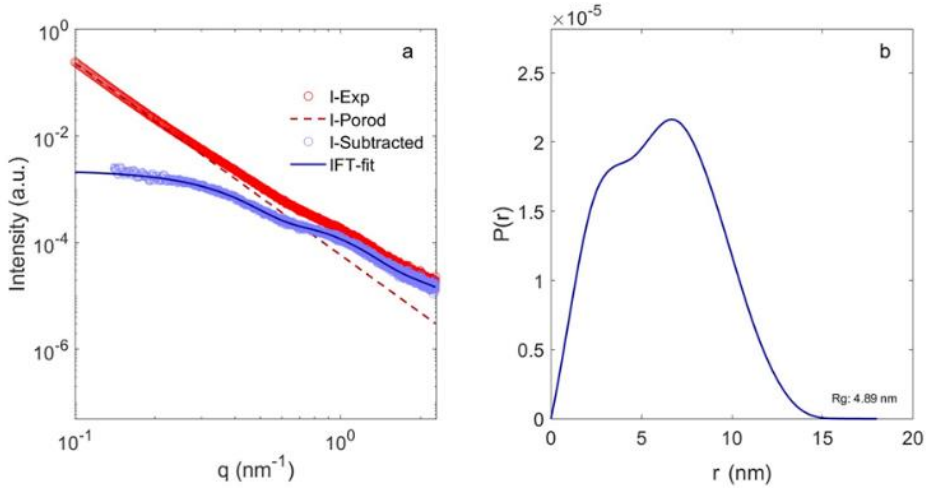

Figure 7. a) Experimental scattering patterns and their relevant residual scattering obtained from subtraction of Porod line are shown together with the indirect Fourier transformation (IFT) evaluation of residual scattering. b) Pair-distance distribution function, $P(r)$, obtained from IFT analysis of residual scattering from pores for the sample 90M10A_CNT-HNO_3_100. (For color, refer to the online version).

The determined radii of gyration by the SAXS study (Figure 6) are significantly lower than the pore sizes estimated by the average pore diameter (P_d) equation ($P_d = 4V_P/S_{BET}$) (Table 1). This discrepancy can be explained by the fact that SAXS is not sensitive to structural features around or larger than 100 nanometers (depending on the instrument

resolution). In other words, the radius of gyration determined by SAXS corresponds to nanometer sized length scales of smaller primary particles, which are not accurately determined by equation (3) or visible by microscopic techniques.

From the SAXS data, a significant reduction of the radius of gyration of pores was observed by the addition of amine groups, with values changing from 22.7 ± 2.52 nm (100M) to 4.89 ± 0.68 nm (90M10A) and 9.33 ± 0.46 nm (80M20A). Then, the addition of CNTs causes only a slight decrease if compared with the 90M10A silica matrix.

3.3 Thermo-mechanical characterization

The effect of the 1D and 2D carbon nanomaterials on the typical thermal insulation of the prepared silica aerogels was assessed through measurement of the thermal conductivity of the monolithic materials, as presented in Table 3.

Table 3: Thermal conductivity of the monolithic silica aerogels without carbon nanostructures and with different amounts of CNTs-HNO_3, CNTs-TMOS and GO.

Amount of carbon nanostructure	Thermal conductivity ($mW.m^{-1}.K^{-1}$)		
	100M_CNTs-HNO_3	90M10A_CNTs-HNO_3	80M20A_CNTs-HNO_3
0 mg [10]	36.8 ± 0.7	44.1 ± 0.3	-
10 mg	35.2 ± 0.1	43.2 ± 0.1	-
50 mg	34.7 ± 0.2	46.9 ± 0.1	67.1 ± 0.2
100 mg	36.4 ± 0.1	48.7 ± 0.1	80.7 ± 0.7
200 mg	43.5 ± 0.1	55.2 ± 0.1	80.6 ± 0.4
	100M_CNTs-TMOS	90M10A_CNTs-TMOS	80M20A_CNTs-TMOS
0 mg [10]	36.8 ± 0.7	44.1 ± 0.3	-
10 mg [10]	31.2 ± 0.1	43.7 ± 0.6	-
50 mg	33.3 ± 0.1	47.3 ± 0.1	62.1 ± 0.5
100 mg	33.1 ± 0.1	47.7 ± 0.1	64.7 ± 0.3
200 mg	36.1 ± 0.1	48.6 ± 0.2	68.2 ± 0.1
		90M10A_GO	80M20A_GO
0 mg	-	48.0 ± 0.1	49.3 ± 0.1
10 mg	-	43.6 ± 0.3	50.0 ± 0.2
50 mg	-	46.3 ± 0.1	49.6 ± 0.1
100 mg	-	45.4 ± 0.1	48.8 ± 0.2

The results in Table 3 indicate that the nature of the silica matrix has a significant impact on the thermal conductivity. It appears that, increasing the amount of APTMS in the system, leads to a significant increase in the values of thermal conductivity, with the samples

containing 20 % of APTMS presenting the highest values. This variation can also be attributed to the higher values of density verified for these samples (Table 1), since thermal conductivity of aerogels highly depend on their bulk density. Several authors [75, 81–84] have demonstrated that this dependence has typically a U-shape, with the solid thermal conductivity being favored by higher densities. On the contrary, the gaseous thermal conductivity has a higher impact for aerogels with lower densities, since the presence of larger pores do not contribute to Knudsen effect [81].

Moreover, the carbon nanostructures also have an impact in the thermal conductivity of the aerogels. The addition of low amounts of the 1D and 2D carbon materials may lead to a reduction in the total thermal conductivity. In the case of CNT-added composites, the most considerable reduction (~ 15 %) was observed for the sample 100M_CNT-TMOS_10, if compared with the corresponding pristine sample. Nevertheless, an increase in the thermal conductivity is observed for all silica systems with the addition of higher quantities of CNTs to the network. This trend can be explained by the potential of percolation threshold in these materials, where the carbon nanostructures increasingly become in contact with each other. Thus, there is an increase in the solid thermal conductivity since preferential paths of heat transfer are formed and CNTs are well known for their high thermal conductivities. Due to the significant shrinkage observed in the 1D carbon-containing composites with higher APTMS content, this effect is most probably enhanced, as observed by SEM imaging (Figure 8), that clearly shows CNTs in close contact with each other.

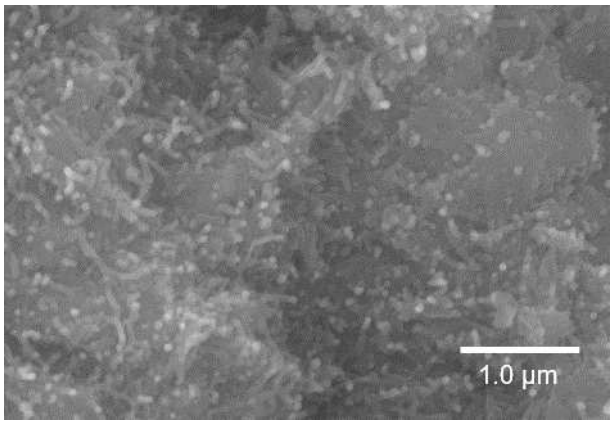

Figure 8. SEM image of the 80M20A aerogels with 200 mg of CNTs-HNO_3.

Considering the different types of surface modification of the CNTs, lower values of thermal conductivity were obtained for the samples with CNTs-TMOS, probably due to the fact that the silica particles grow around these nanotubes, as previously seen in the TEM imaging (Figures 4). Thus, this prevents the contact between the carbon nanotubes and simultaneously alters the silica network, which lead to a reduction of the solid thermal conductivity. The addition of CNTs-HNO_3 also caused a decrease in the thermal conductivity of the CNT-containing composites, probably due to the same reasons. Nonetheless, the found values are higher than those for silanized CNTs, since chemical interaction between the silica network and 1D nanostructures is not so considerable, and it has been verified that these CNTs are further exposed in the aerogel matrix.

As a result of not being able to obtain a cohesive gel for 100 % MTMS, lower values of thermal conductivity were not achieved by the samples with graphene oxide, as the presence of APTMS always causes an increase in this property, as previously mentioned. For the composites made with GO, even though a small reduction in the thermal conductivity is observed for the sample 90M10A_GO_10, the remaining materials all showed very similar values regarding this property. It was expected that the presence of GO would lead to some variability in thermal conductivity, since, with the addition of small amounts of this carbon nanomaterial, a tendency to decrease the thermal conductivity was observed in the literature [6, 16], however, no significant variation was here observed. This can be explained by the pore size of the silica matrix. The reduction in thermal conductivity by the addition of GO occurs because this material makes the pore distribution of the silica matrix more uniform, with a higher number of pores smaller than 70 nm [6, 16], which leads to the constriction of free-molecule-movement. In the case of the silica matrix here developed (MTMS/APTMS using PEG as surfactant), even with addition of GO, the pores do not achieve this low size, always remaining in the macropores range (Table 2 and Figure 5), with the GO even causing the increase of the average pore size in some samples, thus originating an increase of the gaseous contribution to the thermal conductivity.

The effect of temperature on thermal conductivity was determined within a range of temperatures, from -25 ^{o}C to 175 ^{o}C, for the samples 100M and 100M_CNT-TMOS_10, with

the latter being the sample with the lowest value of thermal conductivity (Table 3). The obtained results are illustrated in Figure 9.

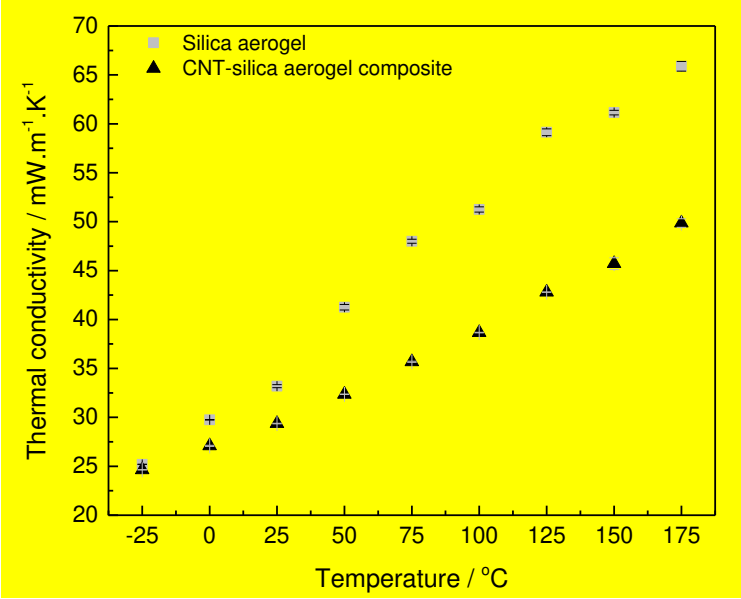

Figure 9. Thermal conductivity of the 100M and 100M_CNT-TMOS_10 aerogels in different temperatures.

As expected, there is a linear increase between temperature and measured thermal conductivity, with the 1D carbon nanostructure-containing composite showing a smaller increase rate. The most significant difference between the two samples was observed when both were submitted to temperatures higher than 75 ºC, with the CNT-silica aerogel composite having thermal conductivity values more than 25 % lower than the ones obtained for the silica aerogel. This difference indicates a significant improvement in the thermal insulation performance of the silica aerogel, as the 100M_CNT-TMOS_10 sample shows lower thermal conductivities in the overall temperature range, especially for temperatures above 50 ºC. This is possibly due to the opacifying effect of CNTs, which limits the radiative contribution on thermal conductivity, as the radiative conductivity becomes increasingly significant at temperatures above 300 K (27 ºC) [75].

Thermal gravimetric analyses were performed for these samples (Figure S5a). Both materials displayed good thermal stability, but, once again, the addition of carbon nanostructures has a positive impact in the properties. The silica aerogel can be applied in

temperatures up to 400 ºC, while the carbon nanotube-silica aerogel composite does not undergo any thermal decomposition until 500 ºC. The addition of amine groups, higher amounts of carbon nanotubes and the type of treatment to which the CNTs were submitted (Figures S5b and S5c) do not have a significant effect in the thermal stability, with the materials being able to be used at temperatures up to 400 ºC. In the case of the graphene oxide-added composites (Figure S5d), a small weight loss is observed before 100 ºC, which is probably due to evaporation of adsorbed water and residual solvents/by-products. After this phenomenon, the samples do not have a thermal decomposition up to 450 ºC, which once again confirms the thermal stability of the developed composites.

The mechanical behavior of the studied silica aerogels and composites was also evaluated by uniaxial compression tests, as shown in Figure 10. For the 100M materials, the Young's modulus is low and approximately the same (in the order of tens of kPa - Table S2) with the most significant variation being observed for the samples with higher amount of CNTs, which showed values of 154 kPa, for the 100M_CNT-HNO_3_200, and 72 kPa, for the 100M_CNT-TMOS_200.

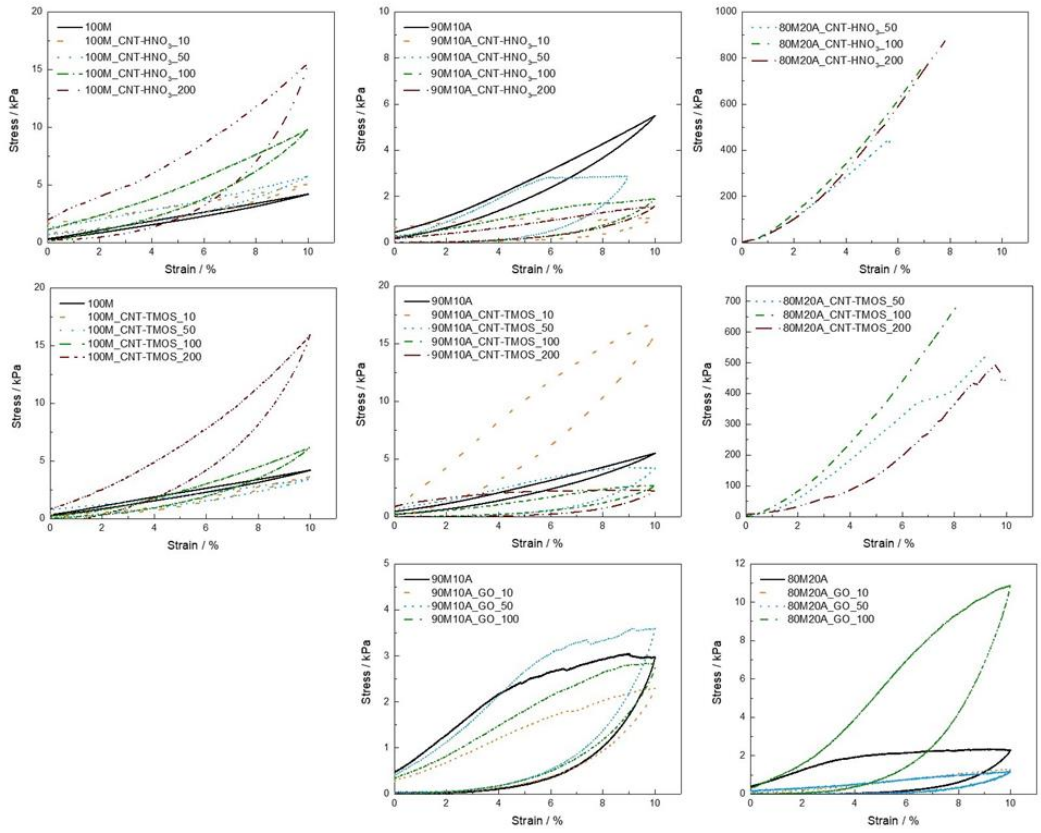

Figure 10. Stress-strain curves for silica aerogels and corresponding carbon nanomaterials-silica aerogel composites obtained by compression-decompression with a load cell of 50 N. (For color, refer to the online version).

Although small variations took place, all the samples are flexible, as they showed high recovery rates. Higher variability is observed for the 90M10A samples with 1D carbon nanostructure, with the Young's modulus appearing to vary randomly. These systems are still relatively flexible, as Young's modulus in the order of tens of kPa were once again obtained, however, these composites have lower recovery rates than the corresponding 100M samples. Even though there are some differences in their microstructure, these samples present larger pores than the other CNTs-containing composites, which can be a possible explanation for these meaningless variations. Besides that, it is also worth mentioning that, due to the inherent variability of the compression tests, these tests are not sensitive enough to detect small variations in the samples structure. For the 80M20A composites with carbon nanotubes, the highest values were obtained, with the Young's modulus in the order of MPa (between 1 and 14 MPa - Table S2), and these results are probably due to the significant shrinkage

observed for these samples during the drying step, and correlated to higher bulk densities. In contrast to what is observed for 100M-based aerogels, these samples are not flexible.

The composite systems with GO present similar mechanical behavior, with Young's modulus values below 50 kPa, except for 80M20A_GO_200 that showed a Young's modulus of 150 kPa. The substantial presence of large pores within these materials is probably the main cause for these findings, since only small variations in the measurements were detected with the addition of GO to the systems. Moreover, these results are also in agreement with the ones obtained for the 90M10A samples with CNTs, which also present pores in the macropore range. The energy absorbing capabilities of the aerogels were also investigated by the cyclic compression tests (Table S3). Low energy losses were obtained for the materials with only MTMS in their matrix, with the lowest values being achieved by the samples 100M and 100M_CNT-TMOS_10, which indicates a small energy dissipation during the load-unload cycles. The larger energy losses observed for the remaining samples probably result from plastic deformation, which agrees with previous results, as these materials do not have good recovery rates after compression.

3.4 Electrochemical characterization

The electrochemical performance of the silica-based aerogels and the corresponding composites with 1D and 2D carbon materials were investigated by CV and EIS. In order to quantitatively evaluate the charge storage capacity, the specific capacitance was determined using equation 5, with the results summarized in Table 4. In general, the presence of amine groups has a significant impact on the specific capacitance, since these systems show higher values than the 100 % MTMS composites.

Table 4: Calculated specific capacitance of silica aerogels without carbon nanostructures and with different amounts of CNTs-HNO_3, CNTs-TMOS and GO from the CV curves at 50 $mV.s^{-1}$.

Amount of carbon nanostructure	Specific capacitance ($\mu A.g^{-1}$)		
	100M_CNTs-HNO_3	90M10A_CNTs-HNO_3	80M20A_CNTs-HNO_3
0 mg	98.3	906.8	184.2
10 mg	222.9	537.4	287.1
50 mg	260.0	519.4	383.7
100 mg	395.8	715.0	434.7
200 mg	1108.9	442.7	943.7
	100M_CNTs-TMOS	90M10A_CNTs-TMOS	80M20A_CNTs-TMOS
0 mg	98.3	906.8	184.2
10 mg	212.0	990.7	287.3
50 mg	242.4	1419.3	340.4
100 mg	566.5	8307.2	635.7
200 mg	877.6	4230.2	701.6
		90M10A_GO	80M20A_GO
0 mg	-	450.1	343.0
10 mg	-	307.1	845.7
50 mg	-	588.6	948.4
100 mg	-	1541.6	1279.2

For most of the systems, increasing the carbon content in the composite leads to an increase in the specific capacitance of the materials. In the 90M10A systems with carbon nanotubes, the variation was not linear, and the highest values for these composites were achieved for an amount of 100 mg of CNTs. These systems also showed the highest values of specific capacitance, and these can be correlated with the different type of porosities, as these samples show significantly larger macropores than the remaining composites with CNTs (Figure 4). Even though smaller pores (micro- and mesopores) can enhance the specific surface area of aerogels, their presence can have a negative effect in the electrical properties. In porous materials, the electrical double layer (EDL) is formed inside the material pores and not adjacent to the electrode surface. Thus, when the pore size is in the same magnitude order as the EDL thickness, the electrical double layers inside the pore overlap, causing a reduction in their electrical capacities [85, 86]. As this overlapping effect exists only in microporous and in a part of mesoporous region, the 90M10A samples do not show this effect, which can explain the superior values obtained for these aerogels. The same explanation can be used for the 2D carbon-containing composites, if compared with their CNTs equivalent, especially for the 80M20A systems, as the composites show significant different average pore sizes

(Tables 1 and 2), which supports the fact that the GO-added composites present higher specific capacitance values.

Regarding EIS analysis presented in Figure 11, the spectra were fitted with the same electrical equivalent circuit consisting of the cell resistance (RΩ - R1) in series with a parallel combination of a constant phase element, (CPE - Q1), and a charge transfer resistance (Rct - R2), as shown in Figure 11. The CPE is assumed as a non-ideal capacitor according to the relation CPE = $-1/(Ci\omega)^{\alpha}$, where C is the capacitance, which describes the charge separation at the double layer interface, ω is the angular frequency and α is the roughness factor (due to heterogeneity of the surface), that varies from 0.5 to 1, where an α value of 1 represents a perfectly smooth surface [87, 88].

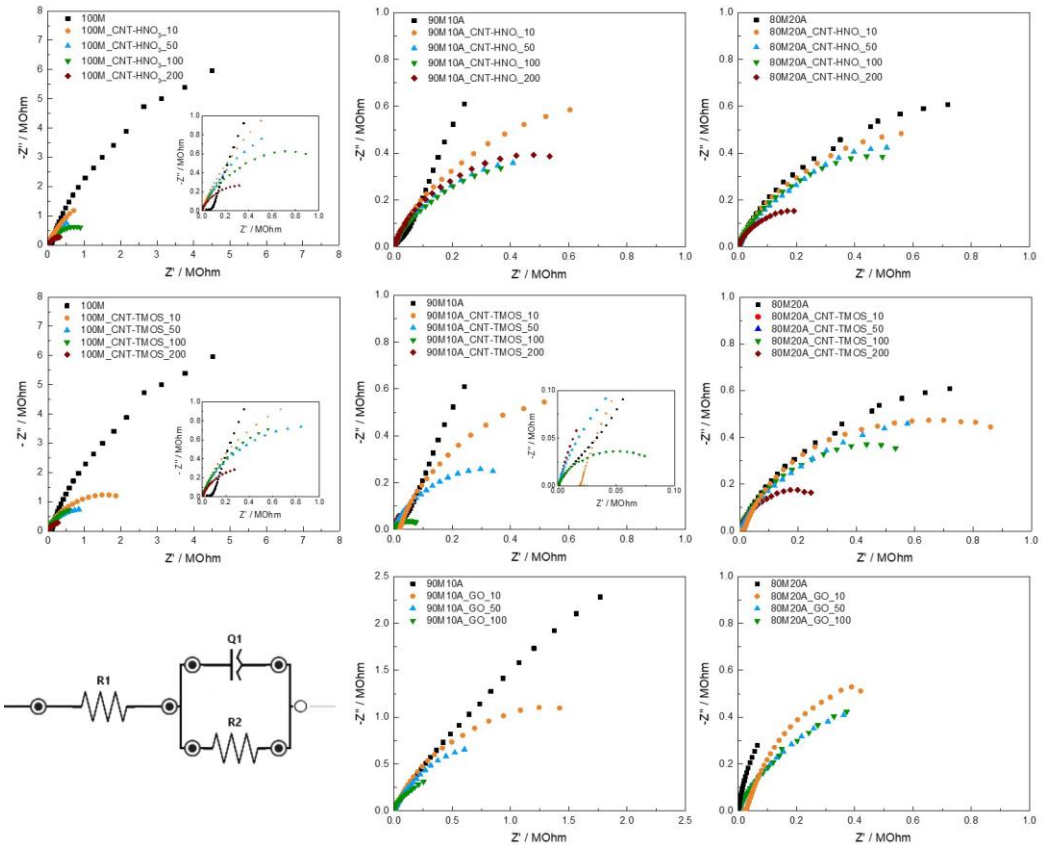

Figure 11. The Nyquist plots of the silica aerogels and carbon nanomaterial-silica aerogel composites electrodes and their equivalent circuit. (For color, refer to the online version).

All EIS Nyquist plots present a single region, a semicircular part, probably corresponding to the electron transfer process. For the electrodes composed of the pristine aerogels, the semicircle shows larger diameters, and, as the semicircle diameter is directly proportional to the resistance of the electrons flow at the interface, these results indicate that in these samples the electron transfer is not very effective. The presence of 1D and 2D carbon nanostructures leads to a decrease of the imaginary part of the impedance (-Z"), suggesting the increase of the capacitance, which in its turn, improves the electrochemical response. This agrees with the results obtained by the cyclic voltammograms for these electrodes.

For most of the systems, as the amount of carbon material increased, further reductions in the impedance were observed, and this decrease indicates that the electrons could be transferred faster with lower loss, which could lead to higher electrochemical performances. These results were expected considering that the carbon nanostructures possess high electrical conductivity and decrease the Rct, allowing a quick electron transfer through the 3D structure. Again, the exception for this continuous decreasing trend in impedance was the 90M10A with CNTs. The samples with 200 mg of CNTs show higher impedance values than those containing 100 mg. These variations are probably due to the materials porosities, as previously discussed regarding the specific capacitances determined by CV. Finally, the presence of amine groups in the silica matrix also caused a significant change in the samples' resistance. The aerogels developed with APTMS present a smaller semicircle than the 100M samples. There are two factors which may explain this difference; first, the different porous structure which may enhance the electron transport at electrode/electrolyte interface leading to higher values of capacitance [89], and second, the introduction of nitrogen which endows the electron donor characteristics and provides electrochemically active sites for pseudo-capacitive reactions [90].

4 CONCLUSIONS

The influence of adding different 1D and 2D carbon nanostructures in the properties of MTMS-based silica aerogels was here evaluated. The composite materials consisting of carbon nanotubes or graphene oxide and silica aerogels have been prepared by using an acid-base-catalyzed sol–gel process. The presence of these carbon materials did not prevent the

formation of the silica three-dimensional network; however, the addition of GO caused more impact in the aerogels' chemical structure than CNTs. The physical properties were also affected by their addition, with variations being observed mainly in the specific surface area and average pore sizes, but the presence of APTMS in the silica matrix proved to be more influential than the carbon nanomaterials.

The CNTs have a more significant impact in the microstructure of the materials than the GO. As observed in SEM and TEM images, the silica matrix can grow around the 1D nanomaterials and follow their shape, especially for the CNTs modified with TMOS. Regarding the thermal properties, it was proven that the presence of GO did not have a meaningful influence in the thermal conductivity, however this is probably due to the presence of pores in the micrometers order, that have a larger impact in this property than the GO. On the other hand, the addition of small amounts of CNTs leads to a decrease in the thermal conductivity of the silica aerogels, with this effect being more significant at temperatures above 50 ◦C. The addition of CNTs also led to an improvement on the aerogels' thermal stability, with the carbon nanotube-silica aerogel composites enduring temperatures up to 500 ºC with negligible thermal decomposition. The combination of these excellent thermal properties indicates that the CNTs-silica aerogel composites have a great potential to be applied in the thermal insulation field, especially in high-temperature environments.

The addition of these carbon nanomaterials also has a significant effect in the electrochemical properties of silica aerogels, leading to an increase in the specific capacitance and a decrease of the resistance of the electrons flow at the interface of these materials. The higher specific capacitances were achieved by the 90M10A systems with 100 mg of CNTs-TMOS and GO. For most of the systems, the lowest resistances were obtained for the composites with the higher amounts of carbon nanostructures, as expected.

In summary, for MTMS-APTMS silica aerogel systems, CNTs have a more significant impact in the aerogels' features than GO, and it is possible to change both the silica matrix and the amount of carbon nanostructure to achieve the desired characteristics. The possibility of tailoring the properties of these materials gives them a wide application potential in different areas, such as thermal insulation, adsorption, and energy related applications.

ASSOCIATED CONTENT

Supporting Information. Figure S1: Photograph of phase separation when CTAB was added into the solution containing ethanol-water as solvent and graphene oxide. Figure S2: SEM images of a) 90M10A_GO_10 and b) 80M20A_GO_10 without surfactant. Table S1: Chemical systems nomenclature, silica precursors proportion, quantities of solvent, catalysts surfactant and carbon nanomaterial used for each sample. Figure S3: ^{1}H–^{29}Si solid-state MAS-NMR spectra of a) 80 % MTMS/20 % APTMS silica aerogels synthesized with CTAB and PEG; b) 90 % MTMS/10 % APTMS silica aerogels synthesized with and without CNTs; c) 80 % MTMS/20 % APTMS silica aerogels synthesized with and without GO. Figure S4: (a,c,e,g) Experimental scattering patterns and their relevant residual scattering obtained from subtraction of Porod line are shown together with the indirect Fourier transformation (IFT) evaluation of residual scattering. (b,d,f,h) Pair-distance distribution function, P(r), obtained from IFT analysis of residual scattering from pores. Figure S5: Thermogravimetric curves for samples a) 100M and 100M_CNT-TMOS_10; b) 90M10A, 90M10A_CNT-TMOS_10 and 90M10A_CNT-TMOS_100; c) 90M10A, 90M10A_CNT-HNO_3_100 and 90M10A_CNT-TMOS_100 and d) 90M10A and 90M10A_GO_10. Table S2: Young's modulus of silica aerogels without carbon nanostructures and with different amounts of CNTs-HNO_3, CNTs-TMOS and GO. Table S3: Energy loss coefficient at 10 % strain of silica aerogels without carbon nanostructures and with different amounts of CNTs-HNO_3, CNTs-TMOS and GO.

ACKNOWLEDGMENT

Alyne Lamy-Mendes acknowledges CNPq (Brazil) for the funding of the PhD fellowship project 234184/2014-0/GDE, under the programme "Ciência sem Fronteiras" and the COST Action AERoGELS (CA18125) for the Short-Term Scientific Mission (STSM) Grant. Ana Violeta Girão is thankful for funding by national funds (OE), through FCT - Fundação para a Ciência e a Tecnologia, I.P., in the scope of the framework contract foreseen in the numbers 4, 5 and 6 of the article 23, of the Decree-Law 57/2016, of August 29, changed by Law 57/2017, of July 19. This work was developed within the scope of the projects CICECO-Aveiro Institute of Materials, UIDB/50011/2020 & UIDP/50011/2020, and CIEPQPF -

Chemical Process Engineering and Forest Products Research Centre projects POCI-01-0145-FEDER-006910 and UID/EQU/00102/2020, financed by national funds through the Portuguese Foundation for Science and Technology/MCTES. We thank Daniel Rentsch for access to the NMR spectrometer, which was funded in part by grant SNF-150638 from the Swiss National Science Foundation.

REFERENCES

1 A. Lamy-Mendes, R. F. Silva and L. Durães. Advances in carbon nanostructure-silica aerogel composites: A review. J. Mater. Chem. A, 2018, 6, 1340-1369.
2 A.C. Pierre and A. Rigacci. SiO2 aerogels. In Aerogels Handbook, ed. M. A. Aegerter, N. Leventis and M. M. Koebel, Springer, 2011, Chapter 1, 21–45.
3 M. M. Shokrieh and R. Rafiee. A review of the mechanical properties of isolated carbon nanotubes and carbon nanotube composites. Mech. Compos. Mater., 2010, 46, 155–172.
4 R. J. Young, I. A. Kinloch, L. Gong and K. S. Novoselov. The mechanics of graphene nanocomposites: a review. Compos. Sci. Technol., 2012, 72, 1459–1476.
5 S. Dervin, Y. Lang, T. Perova, S. H. Hinder and S. C. Pillai. Graphene oxide reinforced high surface area silica aerogels. J. Non-Cryst. Solids, 2017, 465, 31–38.
6 L. Hong-li, H. Xiang, L. Hong-yan, L. Jing and L. Ya-jing. Novel GO/silica composite aerogels with enhanced mechanical and thermal insulation properties prepared at ambient pressure. Ferroelectrics, 2018, 528, 15–21.
7 J. G. Duque, C. E. Hamilton, G. Gupta, S. A. Crooker, J. J. Crochet, A. Mohite, H. Htoon, K. A. D. Obrey, A. M. Dattelbaum and S. K. Doorn. Fluorescent single-walled carbon nanotube aerogels in surfactant-free environments. ACS Nano, 2011, 5, 6686–6694.
8 A. I. Chernov, A. Y. Predein, A. F. Danilyuk, V. L. Kuznetsov, T. V. Larina and E. D. Obraztsova. Optical properties of silica aerogels with embedded multiwalled carbon nanotubes. Phys. Status Solidi B, 2016, 253, 2440–2445.
9 M. Piñero, M. del Mar Mesa-Díaz, D. de los Santos, M. V. Reyes-Peces, J. A. Díaz-Fraile, N. de la Rosa-Fox, L. Esquivias and V. Morales-Florez. Reinforced silica-carbon nanotube monolithic aerogels synthesised by rapid controlled gelation. J. Sol-Gel Sci. Technol., 2018, 86, 391–399.
10 A. Lamy-Mendes, A. V. Girão, R. F. Silva and L. Durães. Polysilsesquioxane-based silica aerogel monoliths with embedded CNTs. Micropor. Mesopor. Mat., 2019, 288, 109575.
11 M. Sachithanadam and S. C. Joshi. Thermal conductivity variations with composition of gelatin-silica aerogel-sodium dodecyl sulfate with functionalized multi-walled carbon nanotube doping in their composites. Int. J. Heat Mass Tran., 2015, 87, 606–615.
12 J. Zhu, H. Ren and Y. Bi. Opacified graphene-doped silica aerogels with controllable thermal conductivity. J. Porous Mater., 2018, 25, 1697–1705.
13 K. Oikawa, K. Toyota, S. Sakatani, Y. Hayashi and H. Takizawa. Facile synthesis and thermal properties of waterglass-based silica xerogel nanocomposites containing reduced graphene oxide. Ceram. Int., 2019, 45, 4201–4207.
14 M. Zhang, Q. Xiao, C. Chen, L. Li and W. Yuan. Developing a heat-insulating composite phase change material with light-to-thermal conversion performance from graphene oxide/silica hybrid aerogel. Appl. Therm. Eng., 2020, 115303.
15 U. K. H. Bangi, M. S. Kavale, S. Baek and H.-H. Park. Synthesis of MWCNTs doped sodium silicate-based aerogels by ambient pressure drying. J. Sol-Gel Sci. Technol., 2012, 62, 201–207.

16 Y. Lei, Z. Hu, B. Cao, X. Chen and H. Song. Enhancements of thermal insulation and mechanical property of silica aerogel monoliths by mixing graphene oxide. Mater. Chem. Phys., 2017, 187, 183–190.
17 M. Koebel, A. Rigacci and P. Achard. Aerogel-based thermal superinsulation: an overview. J. Sol-Gel Sci. Technol., 2012, 63, 315–339.
18 J. Fricke, X. Lu, P. Wang, D. Büttner and U. Heinemann. Optimization of monolithic silica aerogel insulants. Int. J. Heat Mass Transf., 1992, 35, 2305–2309.
19 C. M. R. Almeida, M. E. Ghica and L. Durães. An overview on alumina-silica-based aerogels. Adv. Colloid Interface Sci., 2020, 102189.
20 J. Huang, H. Liu, S. Chen and C. Ding. Hierarchical porous MWCNTs-silica aerogel synthesis for high-efficiency oily water treatment. J. Environ. Chem. Eng., 2016, 4, 3274–3282.
21 T. Sun, Q. Zhuo, X. Liu, Z. Sun, Z. Wu and H. Fan. Hydrophobic silica aerogel reinforced with carbon nanotube for oils removal. J. Porous Mater., 2014, 21, 967–973.
22 D. Loche, L. Malfatti, D. Carboni, V. Alzari, A. Mariani and M. F. Casula. Incorporation of graphene into silica-based aerogels and application for water remediation. RSC Adv., 2016, 6, 66516–66523.
23 S. V. Thakkar, A. Pinna, C. M. Carbonaro, L. Malfatti, P. Guardia, A. Cabot and M. F. Casula. Performance of oil sorbents based on reduced graphene oxide–silica composite aerogels. J. Environ. Chem. Eng., 2020, 8, 103632.
24 J. Meng, Y. Cao, Y. Suo, Y. Liu, J. Zhang and X. Zheng. Facile fabrication of 3D SiO2@graphene aerogel composites as anode material for lithium ion batteries. Electrochim. Acta, 2015, 176, 1001–1009.
25 S. P. Patil, P. Shendye and B. Markert. Mechanical properties and behavior of glass fiber-reinforced silica aerogel nanocomposites: Insights from all-atom simulations. Scr. Mater., 2020, 177, 65–68.
26 A. V. Rao, S. D. Bhagat, H. Hirashima and G. M. Pajonk. Synthesis of flexible silica aerogels using methyltrimethoxysilane (MTMS) precursor. J. Colloid Interface Sci., 2006, 300, 279–285.
27 K. Kanamori, M. Aizawa, K. Nakanishi and T. Hanada. New transparent methylsilsesquioxane aerogels and xerogels with improved mechanical properties. Adv. Mater., 2007, 19, 1589–1593.
28 S. D. Bhagat, C.-S. Oh, Y.-H. Kim, Y.-S. Ahn and J.-G. Yeo. Methyltrimethoxysilane based monolithic silica aerogels via ambient pressure drying. Micropor. Mesopor. Mat., 2007, 100, 350–355.
29 K. Kanamori, Y. Kodera, G. Hayase, K. Nakanishi and T. Hanada. Transition from transparent aerogels to hierarchically porous monoliths in polymethylsilsesquioxane sol–gel system. J. Colloid Interface Sci., 2011, 357, 336–344.
30 L. Durães, M. Ochoa, N. Rocha, R. Patrício, N. Duarte, V. Redondo and A. Portugal. Effect of the drying conditions on the microstructure of silica based xerogels and aerogels. J. Nanosci. Nanotechnol., 2012, 12, 6828– 6834.
31 G. Hayase, K. Kanamori and K. Nakanishi. Structure and properties of polymethylsilsesquioxane aerogels synthesized with surfactant n-hexadecyltrimethylammonium chloride. Micropor. Mesopor. Mat., 2012, 158, 247–252.
32 M. D. Clark, S. Subramanian and R. Krishnamoorti. Understanding surfactant aided aqueous dispersion of multi-walled carbon nanotubes. J. Colloid Interface Sci., 2011, 354, 144–151.
33 W. J. Malfait, S. Zhao, R. Verel, S. Iswar, D. Rentsch, R. Fener, Y. Zhang, B. Milow and M. M. Koebel. Surface chemistry of hydrophobic silica aerogels. Chem. Mater., 2015, 27, 6737–6745.
34 W. J. Malfait, R. Verel and M. M. Koebel. Hydrophobization of silica aerogels: insights from quantitative solid-state NMR spectroscopy. J. Phys. Chem. C, 2014, 118, 25545–25554.

35 G. Hayase, K. Kugimiya, M. Ogawa, Y. Kodera, K. Kanamori and K. Nakanishi. The thermal conductivity of polymethylsilsesquioxane aerogels and xerogels with varied pore sizes for practical application as thermal superinsulators. J. Mater. Chem. A, 2014, 2, 6525–6531.
36 G. Zu, K. Kanamori, T. Shimizu, Y. Zhu, A. Maeno, H. Kaji, K. Nakanishi and J. Shen. Versatile double cross-linking approach to transparent, machinable, super compressible, highly bendable aerogel thermal superinsulators. Chem. Mater., 2018, 30, 2759–2770.
37 J. Bhinder and P. K. Agnihotri. Effect of carbon nanotube doping on the energy dissipation and rate dependent deformation behavior of polyurethane foams. J. Cell. Plast., 2021, 57, 287-311.
38 P. R. Oliveira, A. C. Lamy-Mendes, E. I. P. Rezende, A. S. Mangrich, L. H. Marcolino Junior and M. F. Bergamini. Electrochemical determination of copper ions in spirit drinks using carbon paste electrode modified with biochar. Food Chem., 2015, 171, 426–431.
39 V. D. Nithya, B. Hanitha, S. Surendran, D. Kalpana and R. K. Selvan. Effect of pH on the sonochemical synthesis of BiPO4 nanostructures and its electrochemical properties for pseudocapacitors. Ultrason. Sonochem., 2015, 22, 300–310.
40 A. A. Ensafi, N. Ahmadi and B. Rezaei. Electrochemical preparation of $CuBi_2O_4$ nanoparticles on nanoporous stainless steel as a binder-free supercapacitor electrode. J. Alloys Compd., 2015, 652, 39–47.
41 A. A. Ensafi, N. Ahmadi and B. Rezaei. Electrochemical preparation and characterization of a polypyrrole/nickel-cobalt hexa-cyanoferrate nanocomposite for supercapacitor applications. RSC Adv., 2015, 5, 91448–91456.
42 R. Al-Oweini and H. El-Rassy. Synthesis and Characterization by FTIR Spectroscopy of Silica Aerogels Prepared Using Several Si(OR)4 and R"Si(OR')3 precursors. J. Mol. Struct., 2009, 919, 140–145.
43 K. Krishnamoorthy, M. Veerapandian, K. Yun and S.-J. Kim. The chemical and structural analysis of graphene oxide with different degrees of oxidation. Carbon, 2013, 53, 38 – 49.
44 N. M. S. Hidayah, W.-W. Liu, C.-W. Lai, N. Z. Noriman, C.-S. Khe, U. Hashim and H. C. Lee. Comparison on graphite, graphene oxide and reduced graphene oxide: Synthesis and characterization. In AIP Conference Proceedings, 2017, 1892, 150002. AIP Publishing LLC.
45 N. R. Wilson, P. A. Pandey, R. Beanland, R. J. Young, I. A. Kinloch, L. Gong, Z. Liu, K. Suenaga, J. P. Rourke, S. J. York, et al. Graphene oxide: structural analysis and application as a highly transparent support for electron microscopy. ACS Nano, 2009, 3, 2547–2556.
46 F. L. Galeener. Planar rings in glasses. Solid State Commun., 1982, 44, 1037–1040.
47 C. J. Brinker, D. R. Tallant, E. P. Roth and C. S. Ashley. Sol-gel transition in simple silicates: III. Structural studies during densification. J. Non-Cryst. Solids, 1986, 82, 117–126.
48 B. Humbert, A. Burneau, J. P. Gallas and J. C. Lavalley. Origin of the Raman bands, D1 and D2, in high surface area and vitreous silicas. J. Non-Cryst. Solids, 1992, 143, 75–83.
49 B. Riegel, I. Hartmann, W. Kiefer, J. Groβ and J. Fricke. Raman spectroscopy on silica aerogels. J. Non-Cryst. Solids, 1997, 211, 294–298.
50 C. Kinowski, S. Turrell, M. Bouazaoui, B. Capoen, J.-M. Nedelec and L. L. Hench. Raman spectroscopic investigations of the effects of Ag+ and Ce3+ doping on the densification of nanoporous silica xerogels. J. Sol-Gel Sci. Technol., 2004, 32, 345–348.
51 J. Amonkosolpan, D. Wolverson, B. Goller, S. Polisski, D. Kovalev, M. Rollings, M. D. W. Grogan and T. A. Birks. Porous silicon nanocrystals in a silica aerogel matrix. Nanoscale Res. Lett., 2012, 7, 397.
52 W. J. Malfait. Vibrational properties of glasses and melts, in Magmas Under Pressure, ed. Y. Kono and C. Sanloup, Elsevier, 1st edition, 2018, Chapter 8, 211–236.
53 Z. Li, S. Zhao, M. M. Koebel and W. J. Malfait. Silica aerogels with tailored chemical functionality. Mater. Des., 2020, 108833.

54 S. L. B. Lana and A. B. Seddon. X-ray diffraction studies of sol-gel derived ORMOSILs based on combinations of tetramethoxysilane and trimethoxysilane. J. Sol-Gel Sci. Technol., 1998, 13, 461–466.
55 M. Ochoa, L. Durães, A. M. Beja and A. Portugal. Study of the suitability of silica based xerogels synthesized using ethyltrimethoxysilane and/or methyltrimethoxysilane precursors for aerospace applications. J. Sol-Gel Sci. Technol., 2012, 61, 151–160.
56 D. C. Marcano, D. V. Kosynkin, J. M. Berlin, A. Sinitskii, Z. Sun, A. Slesarev, L. B. Alemany, W. Lu and J. M. Tour. Improved synthesis of graphene oxide. ACS Nano, 2010, 4, 4806–4814.
57 G. Wang, X. Sun, C. Liu and J. Lian. Tailoring oxidation degrees of graphene oxide by simple chemical reactions. Appl. Phys. Lett., 2011, 99, 053114.
58 S. Thangavel and G. Venugopal. Understanding the ad-sorption property of graphene-oxide with different degrees of oxidation levels. Powder Technol., 2014, 257, 141–148.
59 L. Stobinski, B. Lesiak, A. Malolepszy, M. Mazurkiewicz, B. Mierzwa, J. Zemek, P. Jiricek and I. Bieloshapka. Graphene oxide and reduced graphene oxide studied by the XRD, TEM and electron spectroscopy methods. J. Electron Spectros. Relat. Phenomena, 2014, 195, 145–154.
60 F. Y. Ban, S. R. Majid, N. M. Huang and H. N. Lim. Graphene oxide and its electrochemical performance. Int. J. Electrochem. Sci., 2012, 7, 4345–4351.
61 M.-C. Hsiao, S.-H. Liao, M.-Y. Yen, P.-I. Liu, N.-W. Pu, C.-A. Wang and C.-C. M. Ma. Preparation of covalently functionalized graphene using residual oxygen-containing functional groups. ACS Appl. Mater. Interfaces, 2010, 2, 3092–3099.
62 K. Kanamori, M. Aizawa, K. Nakanishi and T. Hanada. Elastic organic–inorganic hybrid aerogels and xerogels. J. Sol-Gel Sci. Technol., 2008, 48, 172–181.
63 K. Kanamori, K. Nakanishi and T. Hanada. Sol-gel synthesis, porous structure, and mechanical property of polymethylsilsesquioxane aerogels. J. Ceram. Soc. Jpn., 2009, 117, 1333–1338.
64 N. Hüsing, U. Schubert, R. Mezei, P. Fratzl, B. Riegel, W. Kiefer, D. Kohler and W. Mader. Formation and structure of gel networks from Si(OEt)4/(MeO)3Si(CH2)3NR‘2 mixtures (NR‘2= NH2 or NHCH2CH2NH2). Chem. Mater., 1999, 11, 451–457.
65 D. W. Schaefer. Polymers, fractals, and ceramic materials. Science, 1989, 243, 1023–1027.
66 A. V. Rao, M. M. Kulkarni, D. P. Amalnerkar and T. Seth. Superhydrophobic silica aerogels based on methyltrimethoxysilane precursor. J. Non-Cryst. Solids, 2003, 330, 187–195.
67 N. H. Borzęcka, B. Nowak, J. M. Gac, T. Głaz and M. Bojarska. Kinetics of MTMS-based aerogel formation by the sol-gel method-experimental results and theoretical description. J. Non-Cryst. Solids, 2020, 547, 120310.
68 H. Bargozin, L. Amirkhani, J. S. Moghaddas and M. M. Ahadian. Synthesis and application of silica aerogel-MWCNT nanocomposites for adsorption of organic pollutants. Sci. Iran., 2010, 17, 122–132.
69 B. Wang, K. Song, Y. Han and T. Zhang. Synthesis and characterization of multi-walled carbon nanotube doped silica aerogels. J. Wuhan Univ. Technol., 2012, 27, 512–515.
70 S. Dervin and S. C. Pillai. An Introduction to Sol-Gel Processing for Aerogels, in Sol-Gel materials for energy, environment and electronic applications, ed. S. C. Pillai and S. Hehir, Springer, 2017, Chapter 1, 1–22.
71 J. P. Vareda, P. Maximiano, L. P. Cunha, A. F. Ferreira, P. N. Simões and L. Durães. Effect of different types of surfactants on the microstructure of methyltrimethoxysilane-derived silica aerogels: A combined experimental and computational approach. J. Colloid Interface Sci., 2018, 512, 64–76.
72 A. V. Rao, N. D. Hegde and P. M. Shewale. Impervious-ness of the hydrophobic silica aerogels against various solvents and acids. Appl. Surf. Sci., 2007, 253, 4137–4141.
73 N. D. Hegde and A. V. Rao. Physical properties of methyltrimethoxysilane based elastic silica aerogels prepared by the two-stage sol-gel process. J. Mater. Sci., 2007, 42, 6965–6971.

74 I. R. Shaikh, N. M. N. Maldar, C. S. Lee, R. C. Pawar, H.-H. Park and U. K.-H. Bangi. MWCNT incorporated silica aerogel prepared by ambient pressure drying: A recyclable catalyst for multi-component synthesis of benzylpyrazolyl coumarin at room temperature. Iran. Chem. Commun., 2018, 6, 19–29.
75 M. A. Aegerter, N. Leventis and M. M. Koebel. Aerogels Handbook. Springer Science & Business Media, 2011.
76 P. Wang, A. Emmerling, W. Tappert, O. Spormann, J. Fricke and H.-G. Haubold. High-temperature and low-temperature supercritical drying of aerogels–structural investigations with SAXS. J. Appl. Crystallogr., 1991, 24, 777–780.
77 P. Cui, J. Lee, E. Hwang and H. Lee. One-pot reduction of graphene oxide at subzero temperatures. Chem. Comm., 2011, 47, 12370–12372.
78 J. Luo, G. Panzarasa, A. Osypova, F. Sorin, F. Spano, R. M. Rossi, A. Sadeghpour and L. F. Boesel. Polyphenols as morphogenetic agents for the controlled synthesis of mesoporous silica nanoparticles. Chem. Mater., 2019, 31, 3192–3200.
79 G. Fritz, A. Bergmann and O. Glatter. Evaluation of small-angle scattering data of charged particles using the generalized indirect Fourier transformation technique. J. Chem. Phys., 2000, 113, 9733–9740.
80 D. Parida, K. A. Salmeia, A. Sadeghpour, S. Zhao, A. K. Maurya, K. I. Assaf, E. Moreau, R. Pauer, S. Lehner, M. Jovic, H. Cordula and S. Gaan. Template-free synthesis of hybrid silica nanoparticle with functionalized mesostructure for efficient methylene blue removal. Mater. Des., 2021, 109494.
81 S. Groult and T. Budtova. Thermal conductivity/structure correlations in thermal super-insulating pectin aerogels. Carbohydr. Polym., 2018, 196, 73–81.
82 J. C. H. Wong, H. Kaymak, S. Brunner and M. M. Koebel. Mechanical properties of monolithic silica aerogels made from polyethoxydisiloxanes. Micropor. Mesopor. Mat., 2014, 183, 23–29.
83 X. Lu, R. Caps, J. Fricke, C. T. Alviso and R. W. Pekala. Correlation between structure and thermal conductivity of organic aerogels. J. Non-Cryst. Solids, 1995, 188, 226–234.
84 N. Hüsing and U. Schubert. Aerogels—airy materials: chemistry, structure, and properties. Angew. Chem. Int. Ed., 1998, 37, 22–45.
85 K.-L. Yang, T.-Y. Ying, S. Yiacoumi, C. Tsouris and E. S. Vittoratos. Electrosorption of ions from aqueous solutions by carbon aerogel: an electrical double-layer model. Langmuir, 2001, 17, 1961–1969.
86 G. Rasines, P. Lavela, C. Macías, M. Haro, C. O. Ania. and J. L. Tirado. Electrochemical response of carbon aerogel electrodes in saline water. J. Electroanal. Chem., 2012, 671, 92–98.
87 C. Gouveia-Caridade and C. M. A. Brett. The influence of Triton-X-100 surfactant on the electroanalysis of lead and cadmium at carbon film electrodes–an electrochemical impedance study. J. Electroanal. Chem., 2006, 592, 113–120.
88 M. M. Barsan, R. C. Carvalho, Y. Zhong, X. Sun and C. M. A. Brett. Carbon nanotube modified carbon cloth electrodes: Characterisation and application as biosensors. Electrochim. Acta, 2012, 85, 203–209.
89 R. Atchudan, T. N. J. I. Edison, S. Perumal and Y. R. Lee. Green synthesis of nitrogen-doped graphitic carbon sheets with use of prunus persica for supercapacitor applications. Appl. Surf. Sci., 2017, 393, 276– 286.
90 M. Mirzaeian, Q. Abbas, D. Gibson and M. Mazur. Effect of nitrogen doping on the electrochemical performance of resorcinol-formaldehyde based carbon aerogels as electrode material for supercapacitor applications. Energy, 2019, 173, 809–819.